



1

2 **The impact of the South-East Madagascar bloom on the oceanic CO₂ sink.**

3

4 Nicolas Metzl¹, Claire Lo Monaco¹, Coraline Leseurre¹, Céline Ridame¹, Jonathan Fin¹,
5 Claude Mignon¹, Marion Gehlen², Thi Tuyet Trang Chau²

6 ¹ Laboratoire LOCEAN/IPSL, Sorbonne Université-CNRS-IRD-MNH, Paris, 75005, Fr

7 ² Laboratoire LSCE/IPSL, CEA-CNRS-UVSQ, Université Paris-Saclay Gif-sur-Yvette, 91191, Fr

8

9 *Correspondence to:* Nicolas Metzl (nicolas.metzl@locean.ipsl.fr)

10

11 **Abstract**

12 We described new sea surface CO₂ observations in the southwestern Indian Ocean obtained in January 2020
13 when a strong bloom event occurred south-east of Madagascar and extended eastward in the oligotrophic Indian
14 Ocean subtropical domain. Compared to previous years (1991-2019) we observed very low fCO₂ and dissolved
15 inorganic carbon concentrations (C_T) in austral summer 2020, indicative of a biologically driven process. In the
16 bloom the anomaly of fCO₂ and C_T reached respectively -33 μatm and -42 μmol.kg⁻¹ whereas no change is
17 observed for alkalinity (A_T). In January 2020 we estimated a local maximum of air-sea CO₂ flux at 27°S of -6.9
18 mmol.m⁻².d⁻¹ (ocean sink) and -4.3 mmol.m⁻².d⁻¹ when averaging the flux in the band 26-30°S. In the domain 25-
19 30°S/50-60°E we estimated that the bloom led to a regional carbon uptake of about -1 TgC.month⁻¹ in January
20 2020 whereas this region was previously recognized as an ocean CO₂ source or near equilibrium during this
21 season. Using a neural network approach that reconstructs the monthly fCO₂ fields we estimated that when the
22 bloom was at peak in December 2019 the CO₂ sink reached -3.1 (±1.0) mmol.m⁻².d⁻¹ in the band 25-30°S, i.e. the
23 model captured the impact of the bloom. Integrated in the domain restricted to 25-30°S/50-60°E the region was a
24 CO₂ sink in December 2019 of -0.8 TgC.month⁻¹ compared to a CO₂ source of +0.12 (± 0.10) TgC.month⁻¹ in
25 December when averaged over the period 1996-2018. Consequently in 2019 this region was a stronger CO₂
26 annual sink of -8.8 TgC.yr⁻¹ compared to -7.0 (±0.5) TgC.yr⁻¹ averaged over 1996-2018. In austral summer
27 2019/2020, the bloom was likely controlled by relatively deep mixed-layer depth during preceding winter (July-
28 September 2019) that would supply macro and/or micro-nutrients as iron to the surface layer to promote the
29 bloom that started in November 2019 in two large rings in the Madagascar Basin. Based on measurements in
30 January 2020, we observed relatively high N₂ fixation rates (up to 18 nmol N.L⁻¹.d⁻¹) suggesting that diazotrophs
31 could play a role on the bloom in the nutrient depleted waters. The bloom event in austral summer 2020, along
32 with the new carbonate system observations, represents a benchmark case for complex biogeochemical model
33 sensitivity studies (including N₂-fixation process and iron supplies) for a better understanding on the origin and
34 termination of this still “mysterious” sporadic bloom and its impact on ocean carbon uptake in the future.

35

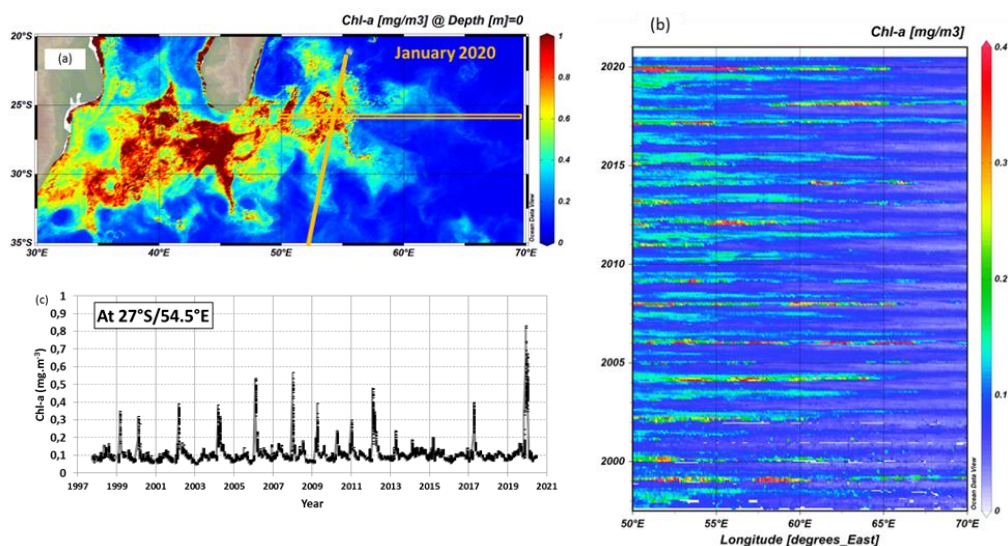
36 **1 Introduction**

37

38 In the south-western subtropical Indian Ocean a phytoplankton bloom, called the South-East
39 Madagascar Bloom (SEMB) occurs sporadically during austral summer (December-March, Figure 1). Based on
40 first years of SeaWiFS satellite Chlorophyll-a (Chl-a) observations in 1997-2001 the SEMB has been first
41 recognized by Longhurst (2001) as the largest bloom in the subtropics, extending over 3000 x 1500 km in the
42 Madagascar Basin. When the SEMB is well developed like in February-March 1999 (Longhurst, 2001), monthly
43 mean Chl-a concentrations are higher than 0.5 mg.m⁻³ within the bloom contrasting with the low Chl-a in the



44 surrounding oligotrophic waters ($< 0.05 \text{ mg}\cdot\text{m}^{-3}$). For reasons still not fully understood, this bloom occurred in
45 specific years (1997, 1999 and 2000) but was absent or moderate during a strong El Niño - Southern Oscillation
46 (ENSO) event in 1998. Following the first study by Longhurst (2001), the frequency, extension, levels of Chl-a
47 concentration and processes that would control the SEMB and its variability have been investigated in several
48 studies (Srokosz et al, 2004; Uz, 2007; Wilson and Qiu 2008; Poulton et al 2009; Raj et al 2010; Huhn et al
49 2012; Srokosz and Quartly 2013). Most of these studies were based on Chl-a derived from remote sensing and
50 altimetry. They all concluded the need for *in-situ* observations to understand the initiation, extend and
51 termination of the SEMB. To our knowledge *in-situ* biogeochemical observations (Chl-a, phytoplanktonic
52 species and nutrients) within the SEMB region were only obtained during the MadEx experiment in February
53 2005 (Poulton et al 2009; Srokosz and Quartly 2013) a year when the bloom was not well developed (e.g. Uz,
54 2007; Wilson and Qiu 2008). The MadEx cruise was conducted above the Madagascar ridge and west of 51°E in
55 the Madagascar Basin. However, the eastward extension of the SEMB reached occasionally the central
56 oligotrophic Indian subtropics (longitude 70°E , Figure 1b) where the bloom is transported and apparently
57 bounded by the South Indian Counter Current (SICC) around 25°S (Siedler et al 2006; Palastanga et al 2007;
58 Huhn et al 2012; Menezes et al 2014). Modelling studies also suggested an eastward propagation of the SEMB
59 through advection or eddy transport originating from the south-east coast of Madagascar (Lévy et al 2007;
60 Srokosz et al 2015; Dilmahamod, et al 2020) but a precise explanation of the internal (e.g. local upwelling,
61 Ekman pumping, meso-scale dynamics) or external processes (e.g. iron from rivers, coastal zones or sediments)
62 at the origin of this “mysterious” bloom is still missing.
63



64
65
66
67 Figure 1: (a): Map of monthly surface Chl-a ($\text{mg}\cdot\text{m}^{-3}$) in the South-Western Indian Ocean in January 2020 derived from
68 MODIS data ($4\times 4\text{km}$ resolution), highlighting the bloom South and South-East of Madagascar. (b) Hovmöller Time-series
69 (Time/Longitude) of Chl-a ($\text{mg}\cdot\text{m}^{-3}$) around 26.5°S along $50\text{-}70^\circ\text{E}$ (Orange box in a). (c) Time-series of monthly Chl-a ($\text{mg}\cdot\text{m}^{-3}$)
70 in the box $27^\circ\text{S}/54.5^\circ\text{E}$ (only when valid number of pixels is greater than 5 for each point). The orange line on the map
71 identifies the track of the OISO-30 cruise. The figures highlight the high Chl-a concentration in austral summer 2020. Figures
72 (a) and (b) produced with ODV (Schlitzer, 2013) from data downloaded at [https://resources.marine.copernicus.eu/](https://resources.marine.copernicus.eu/OCEANCOLOUR_GLO_CHL_L4_REP_OBSERVATIONS_009_093)
73 (OCEANCOLOUR_GLO_CHL_L4_REP_OBSERVATIONS_009_093), last access, 10-April-2021.
74

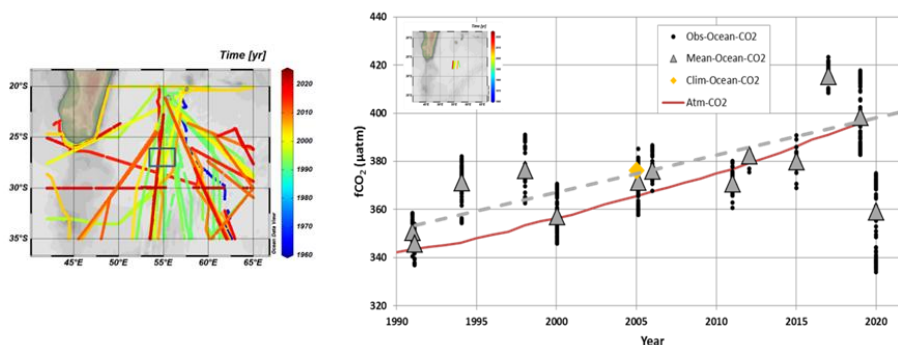
75



76 The above studies have been recently synthesized by Dilmahamod et al (2019) who also proposed an
77 index to determine the level of the SEMB (strong, moderate or absent) based on the difference in Chl-a
78 concentrations between the western and eastern regions centered respectively around 55°E and 80°E at 24-28°S.
79 Quoting Dilmahamod et al (2019): “The South-East Madagascar Bloom is one of the largest blooms in the
80 world. It can play a major role in the fishing industry, as well as capturing carbon dioxide from the atmosphere”.
81 Although numerous cruises measuring sea surface CO₂ fugacity (fCO₂) were conducted since the nineties in the
82 south-western Indian Ocean region (Poisson et al., 1993; Metzl et al., 1995; Sabine et al 2000; Metzl, 2009), the
83 impact of the SEMB on air-sea CO₂ fluxes was not previously investigated. This is probably because the bloom
84 was not strong enough at the time of the cruises to identify large fCO₂ anomalies in this region. Therefore, the
85 temporal (seasonal and/or inter-annual) fCO₂ variability in the western and subtropical Indian Ocean is generally
86 interpreted by thermodynamics as the main control, biological activity and mixing processes being secondary
87 driving processes in this oligotrophic region (Louanchi et al, 1996; Metzl et al 1998; Sabine et al 2000;
88 Takahashi et al 2002). On the other hand, all climatologies based on observations suggest rather homogeneous
89 sea surface fCO₂ or dissolved inorganic carbon (C_T) fields in this region (Takahashi et al, 2002, 2009, 2014; Lee
90 et al, 2000; Sabine et al 2000; Bates et al 2006; Lauvset et al 2016; Zeng et al 2017; Broullón et al 2020; Keppler
91 et al 2020; Fay et al 2021; Gregor and Gruber 2021). This suggests that, although the SEMB and its extent have
92 been regularly observed since 1997 it seems to have a small effect on fCO₂ or C_T spatial variations. However, in
93 austral summer 2019-2020, the SEMB was particularly pronounced reaching monthly mean Chl-a concentrations
94 up to 2.5 mg.m⁻³ at the peak of the bloom in December 2019. It was clearly much stronger than previously
95 observed, at least since 1997 (Figure 1) and reflected in fCO₂ observations in this region (Figure 2).

96 In this analysis, we describe new oceanic carbonate system observations in surface waters obtained in
97 January 2020 associated to this very strong SEMB event and compare these observations with climatological
98 values and previous fCO₂ data when the SEMB was not well developed. We also evaluate the impact of the
99 bloom on air-sea CO₂ fluxes based on both observations and reconstructed monthly fCO₂ fields in the South-
100 Western Indian Ocean.

101
102



103

104

105 Figure 2: Left: Tracks of cruises with sea surface fCO₂ data available in the South-Western Indian Ocean in SOCAT data
106 product (version SOCAT-v2021, Bakker et al, 2016; 2021). Right: Time-series of fCO₂ data (black dots) and mean fCO₂ for
107 each period (grey triangles) in the box 27°S-28°S/55°E (black square in the map and insert on the right) for the months of
108 January and February (data available from 1991 to 2020 for austral summer). The red curve is the atmospheric fCO₂.
109 Although over 1991-2019 the ocean fCO₂ increased by +1.55 (± 0.40) µatm.yr⁻¹ (dashed grey line) due to anthropogenic CO₂
110 uptake, the fCO₂ recorded in January 2020 in the bloom were low compared to previous years with some values below 340
111 µatm, i.e. lower than in 1991. The January-February averaged fCO₂ in the same region derived from the 2005 climatology of
112 Takahasi et al (2014) is also plotted (orange diamond). Map on the left produced with ODV (Schlitzer, 2013).



113

114

115 2 Data collection

116

117 As part of the long-term OISO project (Ocean Indien Service d'Observations), the OISO-30 cruise was
118 conducted in austral summer 2020 (from 2-January to 6-February 2020) onboard the R.V. Marion-Dufresne in
119 the Southern Indian Ocean (part of the track shown in Figure 1). During the cruise, underway continuous surface
120 measurements were obtained for temperature (SST), salinity (SSS), fugacity of CO₂ (fCO₂), total alkalinity (A_T)
121 and total dissolved inorganic carbon (C_T). Analytical methods followed the protocol used since 1998 and
122 previously described for other OISO cruises (e.g. Metzl et al 2006; Metzl, 2009; Lo Monaco et al, 2021). Sea
123 surface temperature and salinity were measured continuously using a SBE45 thermosalinograph. Salinity data
124 were controlled by regular sampling and conductivity measurements (Guildline Autosal 8400B and using IAPSO
125 standard/OSIL). The SST and SSS data were also checked against CTD's surface records when available.
126 Accuracies of SST and SSS are respectively 0.005 °C and 0.01. Total alkalinity (A_T) and total dissolved
127 inorganic carbon (C_T) were measured continuously in surface water (3 to 4 sample/hour) using a potentiometric
128 titration method (Edmond, 1970) in a closed cell. For calibration, we used the Certified Referenced Materials
129 (CRMs, Batch #173) provided by Pr. A. Dickson (SIO, University of California). Replicate measurements were
130 occasionally performed at the same location. At 30°S/54°E for 4 replicates the mean A_T and C_T concentrations
131 were respectively 2328.6 (±0.7) and 1998.2 (±1.6) μmol.kg⁻¹. At 35°S/53.5°E for 6 replicates the mean A_T and
132 C_T were 2340.5 (±0.6) and 2060.6 (±1.1) μmol.kg⁻¹. Overall, we estimated the accuracy for both A_T and C_T
133 better than 3 μmol.kg⁻¹ (based on the analysis of CRMs). Like for all other OISO cruises, the surface underway
134 A_T and C_T data will be available at NCEI/OCADS ([www.ncei.noaa.gov/access/ocean-carbon-data-
135 system/oceans/VOS_Program/OISO.html](http://www.ncei.noaa.gov/access/ocean-carbon-data-system/oceans/VOS_Program/OISO.html)).

136 For fCO₂ measurements, sea-surface water was continuously equilibrated with a "thin film" type
137 equilibrator thermostated with surface seawater (Poisson *et al.*, 1993). The xCO₂ in the dried gas was measured
138 with a non-dispersive infrared analyser (NDIR, Siemens Ultramat 6F). Standard gases for calibration (271.39,
139 350.75 and 489.94 ppm) were measured every 6 hours. To correct xCO₂ dry measurements to fCO₂ *in situ* data,
140 we used polynomials given by Weiss and Price (1980) for vapour pressure and by Copin-Montégut (1988, 1989)
141 for temperature (temperature in the equilibrium cell measured using SBE38 was on average 0.28°C warmer than
142 SST during the OISO-30 cruise). The oceanic fCO₂ data for this cruise are available in the SOCAT data product
143 (version v2021, Bakker *et al.*, 2016, 2021) and at NCEI/OCADS (Lo Monaco and Metzl, 2021). Note that when
144 added to SOCAT, the original fCO₂ data are recomputed (Pfeil *et al.*, 2013) using temperature correction from
145 Takahashi *et al* (1993). Given the small difference between SST and equilibrium temperature, the fCO₂ data
146 from our cruises are identical (within 1 μatm) in SOCAT and NCEI/OCADS. For coherence with other cruises
147 we used the fCO₂ values as provided by SOCAT.

148 During the OISO-30 cruise, silicate (Si) concentrations in surface and water column samples (filtered at
149 0.2 μm, poisoned with 100 μl HgCl₂ and stored at 5°C) were measured onshore by colorimetry (Aminot and
150 Kérouel, 2007; Coverly *et al.* 2009). Based on replicate measurements for deep samples collected during OISO
151 cruises we estimate an error of about 0.3 % in Si concentrations.

152 Unfiltered and 20μm-prefiltered seawater (~ 10m depth) were collected for the determination of net N₂
153 fixation in both the total fraction and the size-fraction lower than 20 μm using the ¹⁵N₂ gas-tracer addition
154 method (Montoya *et al.*, 1996). By difference, we calculated N₂ fixation rates related to the microphytoplankton
155 size class (> 20μm). Immediately after sampling, 2.5ml of 99% ¹⁵N₂ (Eurisotop) were introduced to 2.3L



156 polycarbonate bottles through a butyl septum. $^{15}\text{N}_2$ tracer was added to obtain a ~10% final enrichment. Then,
157 each bottle was vigorously shaken and incubated in an on-deck incubator with circulating seawater and equipped
158 with a blue filter to simulate the level of irradiance at the sampling depth. After 24h-incubation, 2.3L were
159 filtered onto pre-combusted 25mm GF/F filters, and filters were stored at -25°C . Sample filters were dried at
160 40°C for 48h before analysis. Nitrogen (N) content of particulate matter and its ^{15}N isotopic ratio were quantified
161 using an online continuous flow elemental analyzer (Flash 2000 HT), coupled with an Isotopic Ratio Mass
162 Spectrometer (Delta V Advantage via a conflow IV interface from Thermo Fischer Scientific). N_2 fixation rates
163 were calculated by isotope mass balanced as described by Montoya et al. (1996). The detection limit for N_2
164 fixation, calculated from significant enrichment and lowest particulate nitrogen is estimated to $0.04 \text{ nmol N L}^{-1} \text{ d}^{-1}$.
165

166 Other data used in this analysis (e.g. Chl-a from remote sensing, ADCP, current fields, fCO_2 , A_T , C_T
167 from other cruises or from climatology) will be referred to in the next sections when appropriate.
168

169 3 Reconstructed fCO_2 and air-sea CO_2 fluxes

170

171 In order to complement the results based on regional *in-situ* data and evaluate the CO_2 sink anomalies in
172 this region back to 1996, we also used results from a neural network model that reconstructs monthly fCO_2 fields
173 and air-sea CO_2 fluxes. The fCO_2 fields were obtained from an ensemble-based feed-forward neural network
174 model (named CMEMS-LSCE-FFNN) described in Chau et al (2021). To take into account the period in
175 austral summer 2020 when the SEMB was particularly strong, we used the latest temporal extension of the
176 model which relies on the most recent version of the SOCAT data-base (SOCAT-v2021, Bakker et al, 2021). For
177 a full description of the model, access to the data and a statistical evaluation of fCO_2 reconstructions please refer
178 to Chau et al (2021).
179

180

180 4 Results

181

182 4.1 Sea surface fCO_2 , C_T and A_T distributions in the SEMB in January 2020

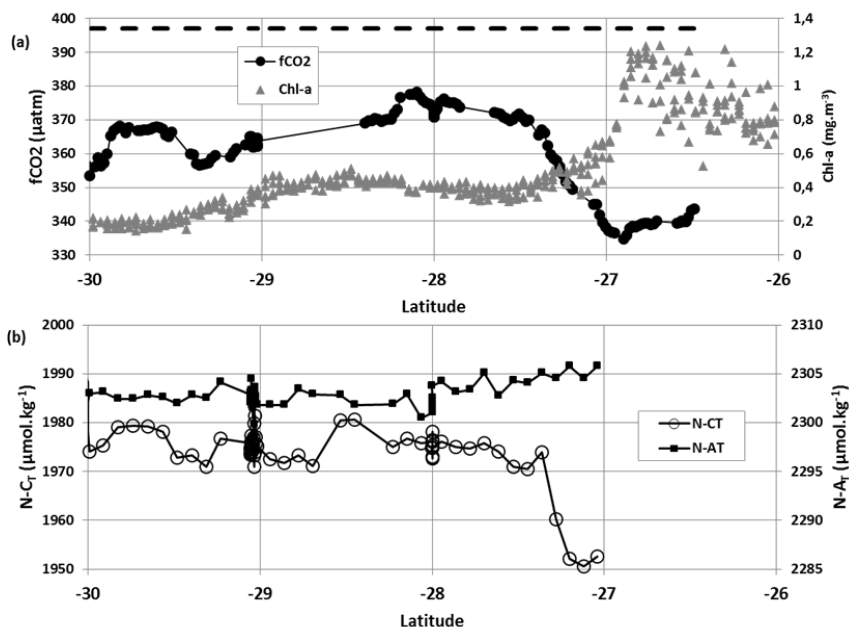
183

184 In January 2020, the SEMB occupied a large region in the Southern section of the Mozambique
185 Channel, the Natal Basin, the Mozambique Plateau and the Madagascar Basin. It extended eastward with meso-
186 scale and filaments structures reaching 60°E in the southern subtropical Indian Ocean where Chl-a was up to 0.5
187 $\text{mg}\cdot\text{m}^{-3}$ (Figure 1a). Compared to previous years, the spatial structure of the 2020 SEMB event resembled to the
188 one that occurred in 2008 (e.g. Dilmahamod et al 2019), albeit with much higher Chl-a concentrations in 2020
189 (Figure 1b, c). As opposed to previous years, the 2020 SEMB event started in November 2019 in the Madagascar
190 Basin and was pronounced in two large rings with monthly mean Chl-a concentrations reaching $1 \text{ mg}\cdot\text{m}^{-3}$ at
191 $25^\circ\text{S}/52^\circ\text{E}$ (Supp Mat Figure S1). These large Chl-a rings were likely linked to eddies and/or to the retroflexion
192 of the South-East Madagascar current, SEMC (Lutjeharms 1988; Longhurst 2001; de Ruijter et al 2004) as seen
193 in the surface currents fields in November 2019 (Supp Mat Figure S2). In December 2019, the surface of the
194 SEMB extended in all directions and a maximum monthly mean Chl-a concentration up to $2.9 \text{ mg}\cdot\text{m}^{-3}$ was
195 detected around $25^\circ\text{S}/51.5^\circ\text{E}$ (Supp Mat Figure S1). The SEMB was less developed in late February 2020 (Supp
196 Mat Figure S1). Whatever the origin and multiple drivers of the SEMB in 2020 through internal or external
197 forcing (Dilmahamod et al 2019) this rather strong biological event would significantly drawdown the C_T
198 concentration and fCO_2 during several weeks from November 2019 to February 2020 in this region.



199 Along the OISO-30 cruise track at 54°E in January 2020, the underway surface measurements started at
200 26.5°S for $f\text{CO}_2$ and at 27°S for A_T and C_T . Along this track the sea surface Chl-a concentrations were relatively
201 lower south of 27°S (0.2-0.4 $\text{mg}\cdot\text{m}^{-3}$) than north of 27°S (0.8-1.2 $\text{mg}\cdot\text{m}^{-3}$, Figure 3a). This was associated with a
202 rapid decrease in $f\text{CO}_2$ (Figure 3a) and salinity normalized C_T ($N-C_T = C_T \cdot 35/\text{SSS}$) concentration (Figure 3b).
203 Because there was a sharp gradient in salinity at that latitude (Supp Mat Fig S3), no significant change was
204 observed for salinity normalized A_T ($N-A_T = A_T \cdot 35/\text{SSS}$) along the track (Figure 3b).

205
206
207
208
209
210
211
212
213
214
215
216
217
218
219
220



221 Figure 3: Top (a): Sea surface $f\text{CO}_2$ (μatm) measured in January 2020 (black circles) and Chl-a ($\text{mg}\cdot\text{m}^{-3}$) from MODIS (4x4
222 km) along the cruise track (grey triangles). Bottom (b): Sea surface salinity normalized C_T ($N-C_T$, open circles) and salinity
223 normalized A_T ($N-A_T$, black squares) measured in January 2020 (both in $\mu\text{mol}\cdot\text{kg}^{-1}$). Low $f\text{CO}_2$ and $N-C_T$ concentrations
224 recorded around 27°S were linked to high Chl-a (up to 1.2 $\text{mg}\cdot\text{m}^{-3}$) in the SEMB. In (a) the dashed-line represents the average
225 atmospheric $f\text{CO}_2$ for January 2020.

226
227
228
229
230
231
232
233
234
235
236
237
238

The mean properties and differences within and out of the peak bloom are listed in Table 1. Although the ocean was warmer in the bloom at 27°S (about +1°C, Supp Mat Fig. S3), $f\text{CO}_2$ was clearly much lower at that location. The $f\text{CO}_2$ difference within and out of the peak bloom was -33 μatm based on $f\text{CO}_2$ measurements. Given the error associated to the $f\text{CO}_2$ calculations using A_T and C_T data (± 13 μatm , Orr et al 2018) the observed $f\text{CO}_2$ difference is confirmed with $f\text{CO}_2$ calculated with the A_T-C_T pairs (difference of -34.5 μatm , last column in Table 1). If one takes into account the effect of the warming on $f\text{CO}_2$ (Takahashi et al, 1993), the $f\text{CO}_2$ in the bloom would be 323.5 μatm . Therefore the solely impact of the biological processes in the bloom reduced $f\text{CO}_2$ by -49.3 μatm . This is a very large effect and coherent with the observed difference in $N-C_T$ of -23.4 $\mu\text{mol}\cdot\text{kg}^{-1}$ within and out of the bloom and almost no change in $N-A_T$ (Table 1).



239
 240 Table 1: Mean properties and their difference observed in January 2020 within and out of the SEMB peak
 241 bloom. For $f\text{CO}_2$, results based on measurements ($f\text{CO}_{2\text{mes}}$) or calculated using A_T - C_T pairs ($f\text{CO}_{2\text{cal}}$) are both
 242 listed. Standard deviations are indicated between brackets.
 243

244 Region	SST 245 °C	SSS 246 PSU	Chl-a 247 $\text{mg}\cdot\text{m}^{-3}$	C_T 248 $\mu\text{mol}\cdot\text{kg}^{-1}$	$N-C_T$ 249 $\mu\text{mol}\cdot\text{kg}^{-1}$	A_T 250 $\mu\text{mol}\cdot\text{kg}^{-1}$	$N-A_T$ 251 $\mu\text{mol}\cdot\text{kg}^{-1}$	$f\text{CO}_{2\text{mes}}$ 252 μatm	$f\text{CO}_{2\text{cal}}$ 253 μatm
248 Within Peak Bloom 249 (Around 27°S)	26.39 (0.21)	35.22 (0.05)	0.97 (0.18)	1958.6 (2.5)	1951.7 (1.0)	2313.5 (2.7)	2305.4 (0.7)	339.5 (2.5)	329.8 (2.0)
251 South of the Peak Bloom 252 (Around 28°S)	25.32 (0.10)	35.48 (0.03)	0.41 (0.04)	2000.6 (2.2)	1975.2 (1.4)	2332.1 (1.9)	2302.4 (1.3)	372.8 (2.2)	364.3 (2.6)
254 Difference In-Out	+1.07	-0.26	+0.56	-42.0	-23.4	-18.6	+3.0	-33.3	-34.5

256
 257
 258 The atmospheric $x\text{CO}_2$ was 410 ppm in January 2020, equivalent to 397 μatm for $f\text{CO}_{2\text{atm}}$ (dashed line
 259 in Figure 3a, where $x\text{CO}_2$ in ppm was corrected to $f\text{CO}_2$ according to Weiss and Price, 1980). Consequently the
 260 region was a strong CO_2 sink within the bloom area with maximal $\Delta f\text{CO}_2$ value of -60 μatm at 27°S (where
 261 $\Delta f\text{CO}_2 = f\text{CO}_{2\text{ocn}} - f\text{CO}_{2\text{atm}}$). As a comparison at this location (28-24°S-52.5°E) the climatological $\Delta f\text{CO}_2$ value for
 262 January (Takahashi et al 2009) was estimated between +4 to +10 μatm , i.e. a small source or near equilibrium. It
 263 is well known that gas exchange at the air-sea interface depends on both $\Delta f\text{CO}_2$ and the wind speed (e.g.
 264 Wanninkhof 2014). The net flux of CO_2 across the air-sea interface ($F\text{CO}_2$) was calculated according to the
 265 following equation (1):

$$266 \quad F\text{CO}_2 = k K_0 \Delta f\text{CO}_2 \quad (\text{Eq. 1})$$

268
 269 Where K_0 is the solubility of CO_2 in seawater calculated from *in situ* temperature and salinity (Weiss, 1974) and
 270 k ($\text{cm}\cdot\text{h}^{-1}$) is the gas transfer velocity expressed from the wind speed U ($\text{m}\cdot\text{s}^{-1}$) (Wanninkhof, 2014) and the
 271 Schmidt number Sc (Wanninkhof, 1992) following equation (2):

$$272 \quad k = 0.251 U^2 (Sc/660)^{-0.5} \quad (\text{Eq. 2})$$

273
 274 In the region 25°S-30°S/45°E-60°E the average monthly wind speed (GMAO, 2015) was 7.9 $\text{m}\cdot\text{s}^{-1}$ in
 275 January 2020. This value is the same as derived from 6-hourly wind speed products at location 27°S-54°E, 7.8
 276 (± 2.3) $\text{m}\cdot\text{s}^{-1}$ (Supp Mat Figure S4a). Using equation (1) and (2), this leads to a CO_2 sink of -6.9 $\text{mmol}\cdot\text{m}^2\cdot\text{d}^{-1}$ at
 277 27°S in January 2020 whereas in the climatology (Takahashi et al 2009) this region was a CO_2 source of +0.72
 278 $\text{mmol}\cdot\text{m}^2\cdot\text{d}^{-1}$ in January. In the band 26-30°S where Chl-a varied between 1.2 and 0.2 $\text{mg}\cdot\text{m}^{-3}$ (Figure 3) the CO_2
 279 sink was still significant on average, -4.3 (± 1.3) $\text{mmol}\cdot\text{m}^2\cdot\text{d}^{-1}$.

280
 281 Integrated over 1 month and a surface of the bloom of 3000x1500 km (Longhurst, 2001), i.e. 4.5 Mkm^2 ,
 282 the carbon uptake in January 2020 would be -7.2 (± 2.2) $\text{TgC}\cdot\text{month}^{-1}$. However, based on the Chl-a distribution
 283 in January 2020 (Figure 1a), we estimated the surface of the bloom east of 45°E to range between 1 and 1.7
 284 Mkm^2 depending the criteria based on Chl-a concentrations (respectively Chl-a = 0.16 $\text{mg}\cdot\text{m}^{-3}$ for a major bloom
 285 or Chl-a = 0.07 $\text{mg}\cdot\text{m}^{-3}$ for a bloom, Dilmahamod et al 2019). This leads to an integrated CO_2 sink ranging
 286 between -1.7 and -2.7 $\text{TgC}\cdot\text{month}^{-1}$ probably more realistic than when using the surface of the bloom as defined
 287 by Longhurst (2001). When restricted to the surface of the domain 25-30°S/50-60°E (0.6 Mkm^2) the integrated
 288 CO_2 sink in January 2020 based on $f\text{CO}_2$ observations would be -1.0 $\text{TgC}\cdot\text{month}^{-1}$.



289 Given the $f\text{CO}_2$ distribution observed in January 2020 and the strong CO_2 sink evaluated within the
290 SEMB, we then compared the 2020 observations with a period when the bloom was absent (or small) and for
291 which $f\text{CO}_2$ data were also available for comparison.

292

293 **4.2 Comparison with a low bloom year: 2005**

294

295 For the period 1998-2016, Dilmahamod et al (2019) synthesized the season and years (their Table 1)
296 with strong or moderate SEMB and years when no bloom was clearly observed, such as in 2005. This is
297 confirmed from the Chl-a time series constructed around 27°S that showed low Chl-a in 2005 compared to 2004
298 and 2006 (Figure 1 b, c). However, it is worth to note that Poulton et al (2009) and Srokosz and Quartly (2013)
299 analyzed in-situ observations collected in this region in February 2005 during the MadEx cruise. They detected
300 that the bloom was present albeit with low Chl-a concentrations (maximum of $0.2 \text{ mg}\cdot\text{m}^{-3}$). Based on surface
301 observations (Chl-a, species and nutrients) along a NE-SE transect between 47°E and 51°E , Srokosz and Quartly
302 (2013) reported that Chl-a variability around 50°E was strongly linked to eddy field as first noticed by Longhurst
303 (2001). They also observed from Seasoar fluorimeter data that the deep chlorophyll maximum (DCM) around
304 70-100m was relatively homogenous along the cruise track and not associated with eddy field as opposed to
305 surface Chl-a. Excepted for silicate that showed some low “patchy” concentrations ($<1 \mu\text{mol}\cdot\text{kg}^{-1}$) associated
306 with filaments of higher Chl-a in the Madagascar Basin (Poulton et al, 2009), no significant variation was
307 observed for other nutrients during MadEx in February 2005 and this was probably the case for $f\text{CO}_2$.

308 Here we revisited the SEMB in austral summer 2005 using data collected during the OISO-12 cruise
309 (expocode 35MF20050113 in the SOCAT data product, Bakker et al, 2016). To compare with 2020, we selected
310 the $f\text{CO}_2$ data collected along the same track around 54°E in February 2005 (note that the $f\text{CO}_2$ data collected in
311 January 2005 to the east, around 60°E , were almost the same, not shown). In the region east of Madagascar, the
312 bloom was discernible around 25°S in January 2005 with maximum Chl-a concentrations around $0.3 \text{ mg}\cdot\text{m}^{-3}$ at
313 50°E (Supp. Mat. Figure S5). In January, the bloom appeared to extend eastward following a large meandering
314 structure around 25°S and in February 2005 the bloom is even detectable at 65°E - 70°E where Chl-a
315 concentration was on average $0.19 (\pm 0.03) \text{ mg}\cdot\text{m}^{-3}$ within the core of the bloom. Interestingly this seems to be
316 centered in the core of the SICC (Huhn et al 2012) as revealed at 25°S by the ADCP observations obtained in
317 2005 along the OISO-12 cruise track as well as in surface current fields (Supp. Mat. Figure S6). Like in
318 November 2019 (Supp. Mat. Figure S2) there was a clear signal of the SEMC retroflexion in January 2005 that
319 could explain the structure and eastward propagation of the bloom.

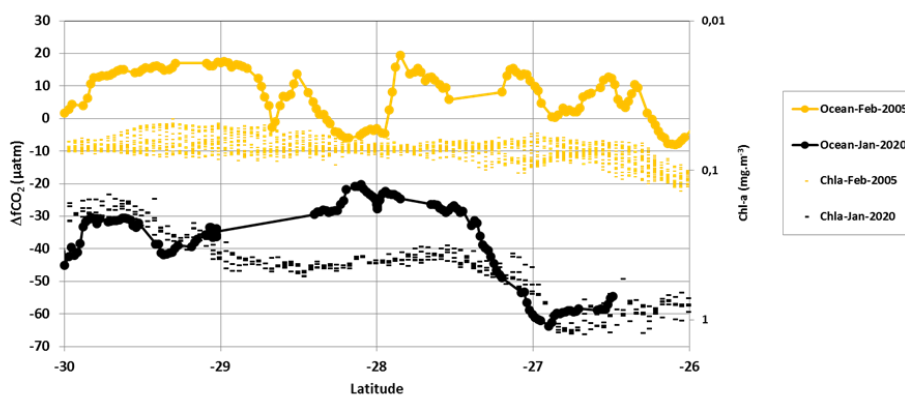
320 The bloom in 2005 was low (Srokosz and Quartly, 2013; Dilmahamod et al, 2019) and thus it had no
321 impact on the $f\text{CO}_2$ distribution. This is shown in Figure 4 where we compared $f\text{CO}_2$ observations along the same
322 track in February 2005 and January 2020. We present the results for $\Delta f\text{CO}_2$ along with sea surface Chl-a for each
323 period. In 2005 the sea surface $f\text{CO}_2$ was pretty homogeneous with values near the atmospheric $f\text{CO}_2$ level
324 ($\Delta f\text{CO}_2$ close to 0). Although one would expect to observe higher $f\text{CO}_2$ 15 years later due to anthropogenic
325 carbon uptake by the ocean driven by the increase in atmospheric CO_2 (and thus about the same $\Delta f\text{CO}_2$), both
326 $f\text{CO}_2$ and $\Delta f\text{CO}_2$ in 2020 were much lower than in 2005 especially north of 27°S (Figure 4, Table 2). In austral
327 summer 2005, the region was near equilibrium with a $\Delta f\text{CO}_2$ mean value of $+8.6 (\pm 7.1) \mu\text{atm}$. This is close to
328 the climatology constructed for a reference year in 2005 (Takahashi et al, 2014, Table 2) and this is expected as
329 the climatology included the $f\text{CO}_2$ data from OISO cruises obtained in this region in 1998-2008. On the opposite,
330 in January 2020 we observed a strong sink (maximum $\Delta f\text{CO}_2 = -60 \mu\text{atm}$ at 27°S). As the temperature was about



331 the same for both periods, the difference in $f\text{CO}_2$ was not due to thermodynamics and the CO_2 sink observed in
 332 2020 was directly linked to the strong SEMB that occurred in austral summer.

333 The average monthly wind speed was also about the same in 2020 (7.9 m.s^{-1}) and 2005 (8.5 m.s^{-1}) (Supp
 334 Mat. Fig S4b). Consequently the difference in the air-sea CO_2 flux between the two periods was controlled by
 335 $\Delta f\text{CO}_2$. In the region $26\text{-}30^\circ\text{S}/55^\circ\text{E}$, the mean CO_2 flux in 2005 was estimated at $+1.2 \text{ mmol.m}^{-2}.\text{d}^{-1}$ (a source)
 336 against $-4.3 \text{ mmol.m}^{-2}.\text{d}^{-1}$ (a sink) in 2020.

337
 338
 339
 340
 341
 342
 343



344
 345
 346
 347

348 Figure 4: $\Delta f\text{CO}_2$ (μatm) ($\Delta f\text{CO}_2 = f\text{CO}_{2\text{ocean}} - f\text{CO}_{2\text{atm}}$) and sea surface Chl-a (mg.m^{-3}) distribution in January 2020 (black) and
 349 February 2005 (orange) along the same track around 54°E in the South-Western Indian Ocean. Here Chl-a is in \log_{10} scale
 350 and inverted. In 2020 when the SEMB was particularly strong $\Delta f\text{CO}_2$ was negative (ocean CO_2 sink), whereas in 2005 when
 351 the bloom was small, $\Delta f\text{CO}_2$ was close to 0 or positive (ocean CO_2 source).

352
 353

354 Table 2: Mean sea surface properties observed along the same track in January 2020 and February 2005 in the
 355 region $30^\circ\text{S}\text{-}26^\circ\text{S}/54^\circ\text{E}$. Also indicated the mean values in the same region and season from the climatology of
 356 Takahashi et al (2014) and the Chl-a climatology evaluated for January-February 1998-2019. Nb is the number
 357 of observations for SST, SSS and $f\text{CO}_2$. Standard deviations are indicated in bracket.

Cruise	Period	SST ($^\circ\text{C}$)	SSS (PSU)	$f\text{CO}_2$ (μatm)	$\Delta f\text{CO}_2$ (μatm)	Chl-a (mg.m^{-3})
OISO-12 Nb= 115	Feb-2005	25.443 (0.813)	35.240 (0.112)	374.2 (7.1)	+8.6 (7.1)	0.087 (0.014)
OISO-30 Nb=217	Jan-2020	25.103 (0.739)	35.442 (0.110)	362.2 (10.7)	-36.2 (10.7)	0.489 (0.266)
Climatology	Jan-Feb	26.242 (0.898)	35.230 (0.140)	376.1 (3.6)	+10.5 (3.6)	0.105 (0.093)

372
 373

5 Discussion

374

5.1 A large biologically driven $f\text{CO}_2$ negative anomaly in 2020 relative to the anthropogenic uptake of CO_2

376

377 Like for $f\text{CO}_2$, the N-C_T concentrations observed in the SEMB in January 2020 ($1950 \mu\text{mol.kg}^{-1}$, Figure
 378 3b, Table 1) were low compared to the climatology (Takahashi et al 2014). At $24^\circ\text{S}\text{-}28^\circ\text{S}/54^\circ\text{E}$, the N-C_T
 379 climatological value in January range between 1970 and 1980 $\mu\text{mol.kg}^{-1}$. As the climatology produced by



380 Takahashi et al (2014) was referred to a nominal year 2005, one would expect to observe higher $N-C_T$
381 concentrations in 2020 due to anthropogenic CO_2 uptake.

382 In the Indian Ocean the decadal change of anthropogenic CO_2 (C_{ant}) was first evaluated by Peng et al
383 (1998) comparing data obtained in 1978 and 1995 north of $20^\circ S$. For the upper layer in the tropics ($20^\circ S-10^\circ S$)
384 Peng et al (1998) estimated an increasing rate of C_{ant} of around $1.1 \mu mol.kg^{-1}.yr^{-1}$. More recently, Murata et al
385 (2010) evaluated the changes of C_{ant} concentrations between 1995 and 2003 in the South Indian Ocean
386 subtropics. They estimated a mean increase of C_{ant} of $+7.9 (\pm 1.1) \mu mol.kg^{-1}$ over 8.5 years in the upper layers
387 that corresponds to a trend of $+0.93 (\pm 0.13) \mu mol.kg^{-1}.yr^{-1}$. In a global context, Gruber et al (2019 a, b)
388 estimated an accumulation of anthropogenic CO_2 (C_{ant}) of $+14.3 (\pm 0.3) \mu mol.kg^{-1}$ in surface waters of the south-
389 western Indian Ocean over 1994-2007, corresponding to an increasing rate in C_{ant} of $+1.10 (\pm 0.02) \mu mol.kg^{-1}.yr^{-1}$.
390 To confirm these C_{ant} trends that were based on the C_{ant} differences between two periods (1995-1978, 2003-
391 1995 or 2007-1994) we calculated the C_{ant} concentrations and long-term trend using water-column data available
392 in 1978-2020 in the region $30-26^\circ S/55^\circ E$. We extracted the data from the most recent GLODAP quality
393 controlled data product (version GLODAPv2-2021, Lauvset et al 2021a,b) completed with data from OISO
394 cruises in 2012-2018. To calculate C_{ant} we used the TrOCA method developed by Touratier et al. (2007).
395 Because indirect methods are not suitable for evaluating C_{ant} concentrations in surface waters due to gas
396 exchange and biological activity we selected the data in the layer 100-250m below the DCM. C_{ant} concentrations
397 were calculated for each sample in that layer and then averaged for each period to estimate the trend (Figure 5).
398 As expected the C_{ant} concentrations in subsurface increased significantly from 1978 to 2020 and the long-term
399 trend of $+1.05 (\pm 0.08) \mu mol.kg^{-1}.yr^{-1}$ over this period is close to previous estimates based on different periods
400 and approaches (Peng et al 1998; Murata et al, 2010; Gruber et al, 2019a).

401

402

403

404

405

406

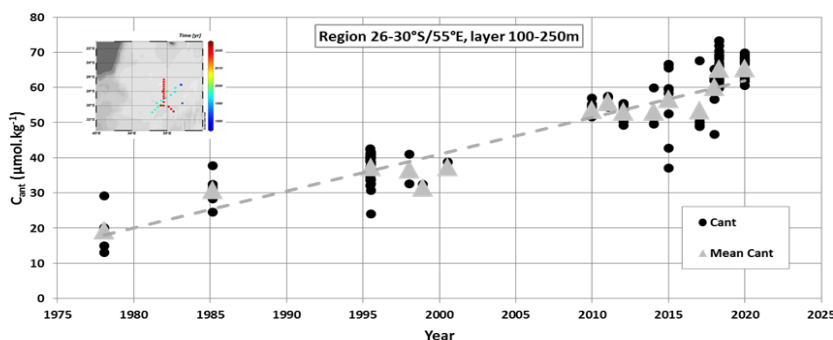
407

408

409

410

411



411

412 Figure 5: Time-series of anthropogenic CO_2 concentrations (C_{ant}) estimated in subsurface (layer 100-250m) in the region 26-
413 $30^\circ S/55^\circ E$ from the GLODAPv2-2021 data product (Lauvset et al, 2021,a,b) completed with OISO cruises in 2012-2018
414 (location of selected stations in the insert map). The figure shows the C_{ant} concentrations calculated for each sample (black
415 dots) and the C_{ant} averaged in the layer 100-250m for each period (grey triangles). Over the period 1978-2020, the C_{ant} long-
416 term trend is $+1.05 (\pm 0.08) \mu mol.kg^{-1}.yr^{-1}$ (dashed grey line).

417

418 Furthermore the C_{ant} trend of around $+1 \mu mol.kg^{-1}.yr^{-1}$ is coherent with an increase in C_T of between
419 $+0.93$ and $+1.17 \mu mol.kg^{-1}.yr^{-1}$ derived from the oceanic fCO_2 increase over the period 1991-2007 estimated
420 from winter and summer fCO_2 data ($+1.75$ and $+2.2 \mu atm.yr^{-1}$ respectively, Metzl, 2009) assuming constant
421 alkalinity and temperature. With the new data available after 2007, we have revisited the fCO_2 long-term trend
422 by selecting only the austral summer data in the region around $27^\circ S-55^\circ E$ (Figure 2). For the period 1991-2019



423 we estimated a $f\text{CO}_2$ trend of $+1.55 (\pm 0.40) \mu\text{atm.yr}^{-1}$. This is less than the atmospheric $f\text{CO}_2$ increase of $+1.89$
424 $(\pm 0.03) \mu\text{atm.yr}^{-1}$ over the same period suggesting that the CO_2 sink increased at this location. In a broader
425 context, Landschützer et al (2016) suggested that the carbon uptake tended to increase slightly in 1998-2011 in
426 the Subtropical Indian Ocean (their figure 3). We will see that such a change in the CO_2 fluxes in this region is
427 also revealed in the CMEMS-LSCE-FFNN model (Chau et al, 2021). Note that if at that location $27^\circ\text{S}/55^\circ\text{E}$
428 (Figure 2) the ocean $f\text{CO}_2$ data in 2020 were also used to estimate the trend (1991-2020), the rate of $f\text{CO}_2$ would
429 be only $+1.09 (\pm 0.48) \mu\text{atm.yr}^{-1}$. i.e. about half the atmospheric $f\text{CO}_2$ trend. The $f\text{CO}_2$ observations in 2020
430 represent a large negative anomaly at local scale and thus caution is needed when incorporating such an anomaly
431 to detect and interpret long-term change in the CO_2 sink, at least in the south-western Subtropical Indian Ocean.

432 To compare the $f\text{CO}_2$ trends listed above with the anthropogenic rate of around $+1.0 \mu\text{mol.kg}^{-1}.\text{yr}^{-1}$
433 (Figure 5), we have calculated C_T from the $f\text{CO}_2$ data and A_T derived from salinity (described below). For this
434 calculation we used the CO2sys program (version CO2sys_v2.5, Orr et al., 2018) developed by Lewis and
435 Wallace (1998) and adapted by Pierrot et al. (2006) with K1 and K2 dissociation constants from Lueker et al.
436 (2000) and KSO_4 constant from Dickson (1990). The total boron concentration is calculated according to
437 Uppström (1974). For nutrients we fixed phosphate concentrations at 0 and silicate at $2.0 (\pm 0.6) \mu\text{mol.kg}^{-1}$ (the
438 mean of 79 surface observations measured during previous OISO cruises in the region 22°S - 30°S). To derive A_T
439 from salinity we used the surface A_T observations obtained since 1998 in the subtropical south-western Indian
440 Ocean (OISO cruises). From these data we estimated a robust relationship (Figure 6):

441

442
$$A_T (\mu\text{mol.kg}^{-1}) = 62.1601 * \text{SSS} + 123.1 \text{ (rms} = 7.0 \mu\text{mol.kg}^{-1}, r = 0.89, n = 3400) \quad (\text{Eq. 3})$$

443

444

445

446

447

448

449

450

451

452

453

454

455

456

457

458

459

460

461

462

463

464

465

466

467

468

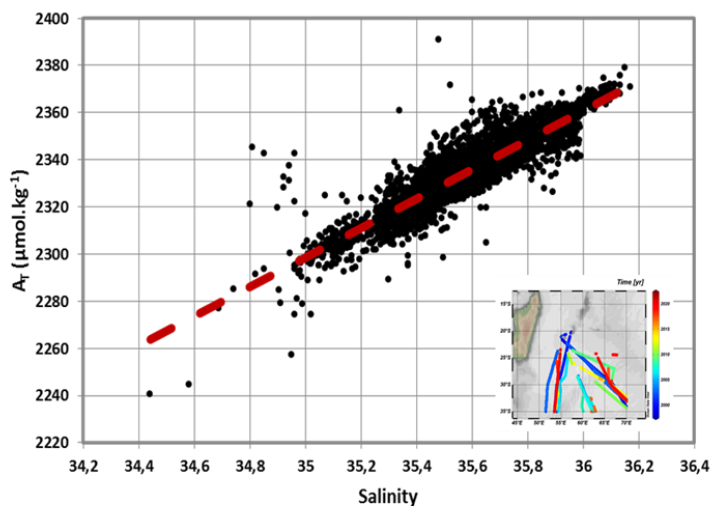
469

470

471

472

473



467 Figure 6: Relationship of A_T ($\mu\text{mol.kg}^{-1}$) versus Salinity deduced from surface A_T data ($n = 3400$) obtained during OISO
468 cruises in 1998-2020 in the South-Western Indian Ocean. For the subtropics we have selected the data in the region 35°S -
469 $20^\circ\text{S}/50^\circ\text{E}$ - 70°E (track of cruises shown in the insert map). The relationship (red dashed) is $A_T = 62.1601 * \text{SSS} + 123.1$ and
470 is used to calculate C_T concentrations in this region (Figure 7). A_T data are available at NCEI/OCADS
471 (https://www.ncei.noaa.gov/access/ocean-carbon-data-system/oceans/VOS_Program/OISO.html).

472

473

474

475

The use of other relationships (e.g. Millero et al 1998; Lee et al 2006) would change slightly the A_T concentrations but not the interpretation on the C_T trend in this region. The time-series of salinity normalized C_T



476 (N-C_T = C_T*35/SSS) in the box 27°S-28°S/55°E shows that N-C_T increased over the period 1991-2019 at a rate
477 of +0.70 (± 0.24) μmol.kg⁻¹.yr⁻¹ (Figure 7). This is somehow lower than the anthropogenic trend of +1 μmol.kg⁻¹.yr⁻¹
478 suggesting that in addition to the anthropogenic CO₂ uptake, natural processes could also have a small
479 impact on the C_T and fCO₂ trends in surface waters over almost 30 years.

480

481

482

483

484

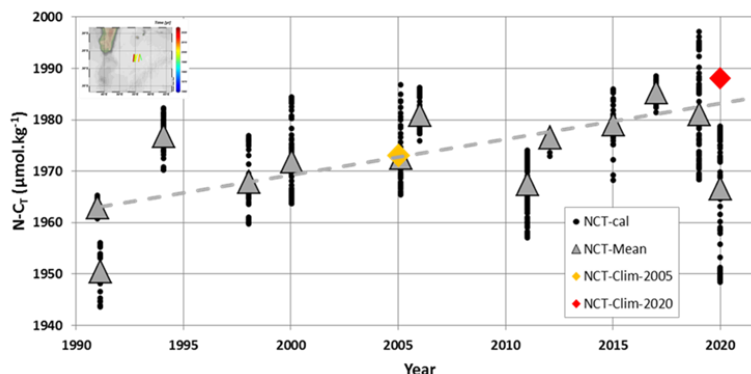
485

486

487

488

489



490 Figure 7: Time-series of salinity normalized C_T (N-C_T black dots) and their monthly mean (grey triangles) in the box 27°S-
491 28°S/55°E (insert map) calculated with fCO₂ observations (see figure 2) and reconstructed A_T from salinity (Figure 6). The
492 figure shows data for the months of January and February (data available from 1991 to 2020 for austral summer). Over the
493 period 1991-2019, the N-C_T trend is +0.70 (± 0.24) μmol.kg⁻¹.yr⁻¹ (dashed grey line) reflecting in part the anthropogenic CO₂
494 uptake. Note the low N-C_T in January 2020 in the SEMB compared to previous years with some values around 1950
495 μmol.kg⁻¹ in 2020 as low as N-C_T calculated in 1991. The N-C_T concentration in the same region derived from the
496 climatology of Takahashi et al (2014) is also plotted (orange diamond for the reference year 2005) as well as the
497 climatological value for year 2020 after correcting for anthropogenic CO₂ (red diamond).

498

499 Having an estimate of the C_T change due to anthropogenic CO₂ (around +1 μmol.kg⁻¹.yr⁻¹) and taking
500 into account this effect, the climatological N-C_T concentration of 1973 μmol.kg⁻¹ for 2005 (Takahashi et al 2014)
501 corrected for the year 2020 would be 1988 μmol.kg⁻¹ in the region of interest. This is higher by up to +36
502 μmol.kg⁻¹ than the observed N-C_T in January 2020 in the SEMB (Table 1, Figure 7). When correcting the
503 climatological value to the observed C_T trend of +0.7 μmol.kg⁻¹.yr⁻¹, the N-C_T in 2020 would be 1983.5 μmol.kg⁻¹,
504 i.e. +32.5 μmol.kg⁻¹ higher than the observed value in January 2020. The N-C_T anomaly in January 2020 is
505 also large compared to the mean N-C_T seasonal amplitude of 20 μmol.kg⁻¹ generally observed in the South
506 Indian subtropics (Metzl et al 1998; Takahashi et al 2014). We also note that climatological N-A_T concentrations
507 of 2295 μmol.kg⁻¹ for January (Takahashi et al 2014) are very close to those we observed in January 2020 (Table
508 1, Figure 3b). Therefore the low fCO₂ and strong CO₂ sink in 2020 in the SEMB is due to a large drawdown of
509 C_T, i.e. not driven by temperature changes or alkalinity.

510

511 5.2 Specificities of the SEMB bloom in 2020

512

513 Based on previous studies it is likely that the biologically driven reduction of C_T in the SEMB under
514 depleted sea surface nitrate concentrations was associated with the process of N₂ fixation (Uz, 2007). The
515 hypothesis that diazotrophy would play a role in the temporal C_T (and thus fCO₂) variability is supported by the
516 observation of large N₂-fixing phytoplankton in the SEMB region in 2005 during MadEx cruise (Poulton et al
517 2009). These authors found that the filamentous cyanobacteria *Trichodesmium* was most abundant south of



518 Madagascar (over the Madagascar ridge) whereas diatom-diazotroph associations (as *Rhizosolenia/Richelia*)
519 were mainly observed east of Madagascar (in the Madagascar Basin).

520 Our measurements in January 2020 showed high spatial variability of the N_2 fixation rate (range from
521 0.8 to 18.3 $\text{nmol N.L}^{-1}.\text{d}^{-1}$, Figure 8). Such variability in the subtropical Indian ocean was also recently reported
522 by Hörstmann et al (2021) who measured N_2 fixation rates between 0.7 and 7.9 $\text{nmol N.L}^{-1}.\text{d}^{-1}$ in January-
523 February 2017 in the same region (OISO-27 cruise) but when the SEMB was not pronounced (Figure 1 b, c) and
524 when $f\text{CO}_2$ was high and above equilibrium (Figure 2). Our results for silicate (Si) and N_2 -fix observations are
525 difficult to interpret because few samples were collected along the track (Figure 8). A maximum of N_2 fixation
526 rate was observed at 30°S that was not linked to changes in other properties. This local high N_2 fixation rate
527 could be related to *Trichodesmium* species but it was not sampled in January 2020. We also noted low Si
528 concentrations at 27°S ($0.6 \mu\text{mol.kg}^{-1}$) associated with higher Chl-a and lower $f\text{CO}_2$ and C_T (Figure 3). The low
529 silicate might be associated with the presence of diatom-diazotroph associations (DDA) as observed during the
530 MadEx cruise (Poulton et al 2009). In the bloom N_2 fixation increased northward from 28°S (factor ~5). Based
531 on measurements for different size fractions we observed that the N_2 fixation is mainly related to the fraction >
532 $20\mu\text{m}$ (i.e. *Trichodesmium* and DDA) representing 88% ($\pm 9\%$) of the N_2 fixation. “Hotspots” of large
533 diazotrophs (20-180 and 180-2000 μm) were also detected in other regions of the south-western Indian Ocean in
534 May 2010 during the TARA expedition (Pierella Karlusich et al, 2021).

535

536

537

538

539

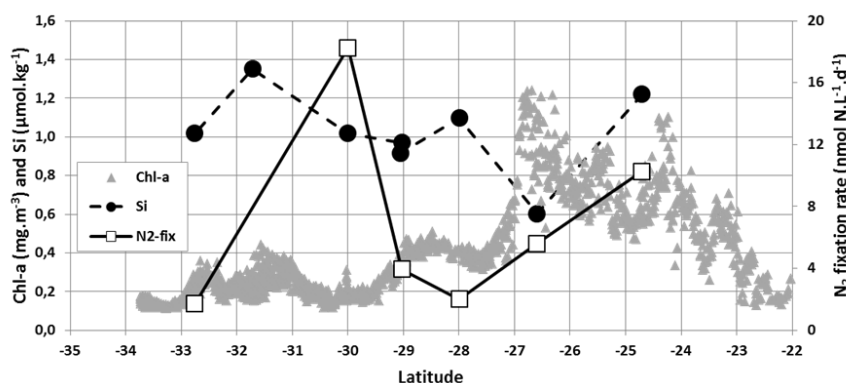
540

541

542

543

544



545

546

547

548

549

550

551

552

553

554

555

556

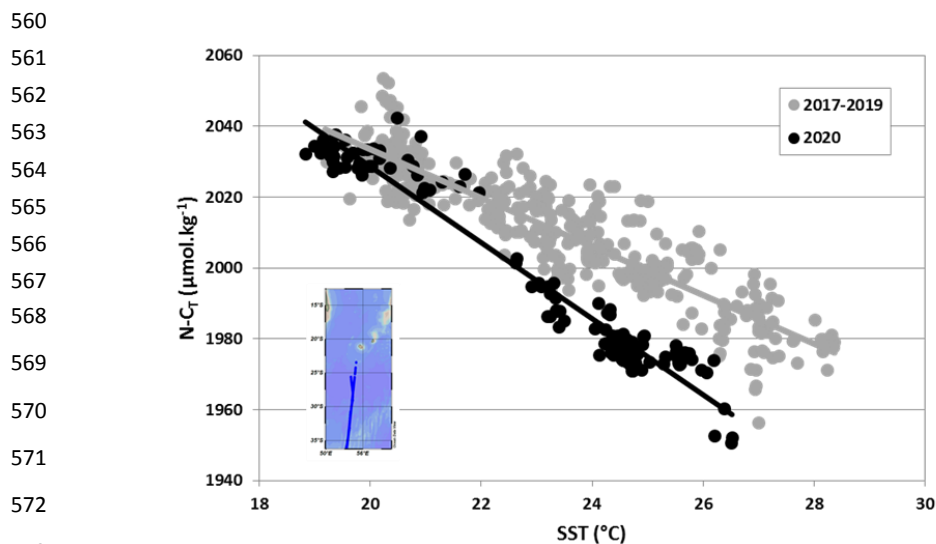
557

558

559

Figure 8: Sea surface silicate concentration (Si, $\mu\text{mol.kg}^{-1}$, black circles, scale on the left), N_2 fixation rate (N_2 -fix, $\text{nmol N.L}^{-1}.\text{d}^{-1}$, open squares, scale on the right) measured in January 2020 (OISO-30 cruise) and Chl-a (mg.m^{-3} , grey triangles, scale on the left) from MODIS (4x4 km) along the cruise track. The low Si concentration ($0.6 \mu\text{mol.kg}^{-1}$) recorded around 27°S was linked to higher Chl-a (up to 1.2mg.m^{-3}) in the SEMB.

At global scale, the presence of N_2 -fixers in the south-western Indian Ocean has been detected from satellite data (Westberry and Siegel, 2006; Qi et al 2020) and relatively high N_2 fixation rates in austral summer in this region were also derived from N_2 -fix data using a machine learning approach (Tang and Cassar, 2019; Tang et al, 2019). A large scale distribution of diazotrophy was further estimated from surface C_T observations suggesting the presence of N_2 -fixers in the Mozambique Channel and the South-Western Indian Ocean (Lee et al, 2002; Ko et al, 2018). These authors used regional $N-C_T$ versus SST relationships to reconstruct the $N-C_T$ field from which they estimated the net carbon production (NCP) in nitrate depleted waters, a proxy for carbon production by N_2 fixing microorganisms. The $N-C_T$ /SST relationship observed from in-situ data in January 2020 somehow mimics this process (Figure 9), i.e. the inter-annual variability of the $N-C_T$ /SST relationship would also inform on the NCP by N_2 -fixers.



574 Figure 9: The relationship between $N-C_T$ ($\mu\text{mol.kg}^{-1}$) and SST in surface waters based on OISO cruises observations in the
575 south-western Indian Ocean in austral summer 2017, 2018, 2019 and 2020 along the same repeated track (insert map). In
576 January 2020 during the strong SEMB the $N-C_T$ /SST relationship (black dots and black line) was much sharper than in 2017-
577 2019 (grey dots and grey line) indicative of N_2 -fix production in nitrate depleted waters (e.g. Ko et al 2018).

578
579 Sea surface warming and shallow mixed-layer depth (MLD) are proposed to lead to optimal conditions
580 for the growth of the N_2 -fixers and generate the SEMB (e.g. Longhurst, 2001; Srokosz et al 2015). In austral
581 summer 2020, the ocean was not much warmer than previous years suggesting that temperature was not a
582 specific driver of the SEMB that year. To the contrary, in January 2020 the region experienced a particularly
583 shallow MLD which might have favored the bloom (observed MLD around 20m at 27°S-28°S, Supp. Mat.
584 Figures S7 and S8).

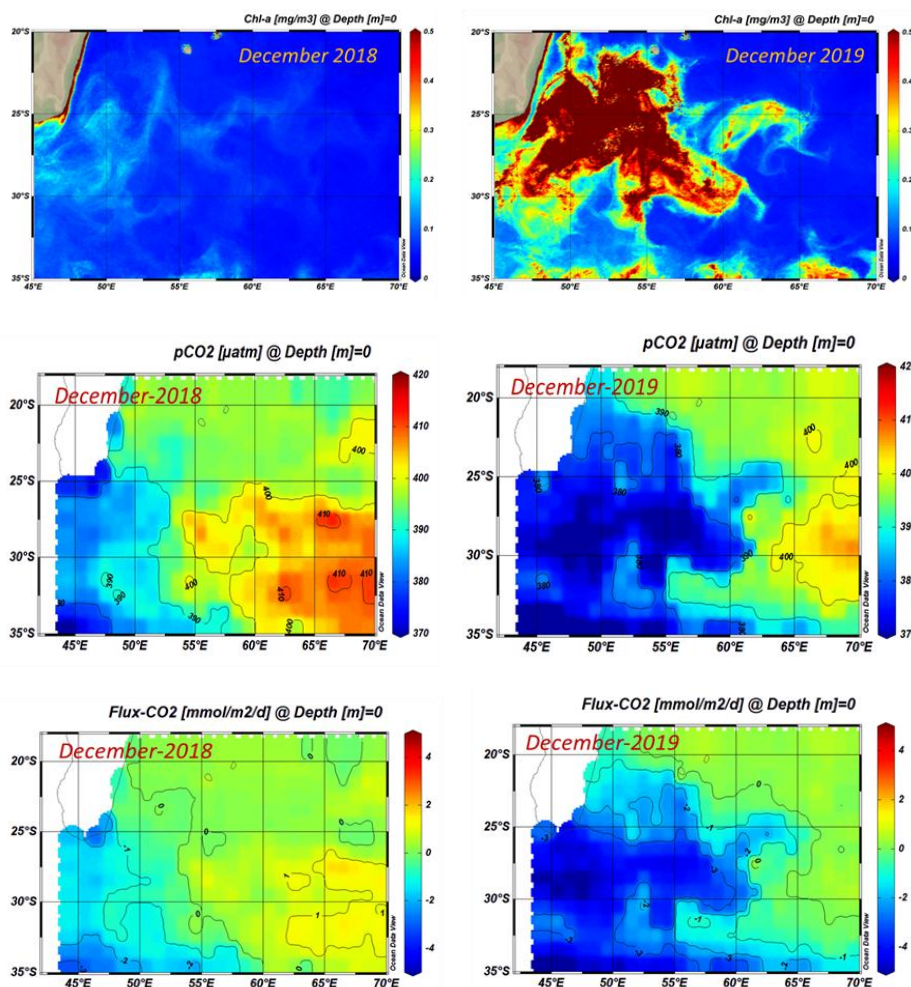
585 As noted above, the strong bloom started in November 2019 and could be well identified in two large
586 rings (Supp. Mat. Figure S1). In the northern ring at 25°S-52°E the MLD was deep ($> 80\text{m}$) during 3 consecutive
587 months in July-September 2019 and deeper compared to previous years (Supp. Mat. Figure S9). This would have
588 injected nutrients (and maybe iron) in surface layers and when the MLD was shallow at that location ($< 20\text{m}$)
589 the bloom developed in November 2019 and reached high Chl-a in December 2019 (up to 1.8 mg.m^{-3}). As the
590 bloom covered a large region in December 2019 and January 2020 other specific processes like iron supply
591 (from dust, coastal zone, rivers or sediments) still need to be identified to fully explain 2020 SEMB dynamics.
592 The 2020 bloom was clearly recognized in Chl-a, $f\text{CO}_2$ and C_T observations but at that stage we have no clear
593 explanation on the process (or multiple drivers) that generated its extend and intensity.

594 5.3 The changing ocean CO_2 uptake in the SEMB based on reconstructed pCO_2

595
596
597 The results presented above were based on local underway $f\text{CO}_2$ observations and the integrated air-sea
598 CO_2 fluxes were thus extrapolated from local data on a surface representing the area covered by the bloom
599 leading to a carbon uptake of between -1.7 and $-2.7\text{ TgC.month}^{-1}$ in January 2020. In the domain 25-30°S/50-
600 60°E we estimated a CO_2 sink in January 2020 close to -1 TgC.month^{-1} .



601 To evaluate the impact of the bloom at the regional scale, we used monthly surface ocean pCO₂ and air-
602 sea CO₂ flux fields reconstructed by a neural network method as described in section 3 (CMEMS-LSCE-FFNN,
603 Chau et al, 2021). The SEMB was well developed in December 2019 and we can evaluate its impact on the air-
604 sea CO₂ fluxes by comparing December 2018 (low bloom) and December 2019 (strong bloom, Figure 10).
605



606
607 Figure 10: Maps of Chl-a (mg.m⁻³), pCO₂ (μatm) and the air-sea CO₂ fluxes (mmol.m⁻².d⁻¹) in the South-Western Indian
608 Ocean in December 2018 (left) and December 2019 (right). In December 2019 when the SEMB was particularly strong, the
609 pCO₂ was lower and air-sea CO₂ fluxes were negative (ocean sink, in blue), whereas in December 2018 when the bloom
610 was small, the fluxes were near equilibrium or positive in this region (ocean source, green-red). Chl-a data downloaded at
611 <https://resources.marine.copernicus.eu/> (OCEANCOLOUR_GLO_CHL_L4_REP_OBSERVATIONS_009_093), last access,
612 10-April-2021. Figures produced with ODV (Schlitzer, 2013)

613
614 In the region 25-30°S/50-60°E, the average pCO₂ in December 2019 (375.9 ±6.3 μatm) was much lower
615 than in December 2018 (396.6 ±6.0 μatm) and thus opposite of the expected pCO₂ increase due to anthropogenic
616 CO₂ uptake. At the local scale, within the bloom at 27°S-54°E or at 29°S-50°E the CMEMS-LSCE-FFNN model
617 estimated low pCO₂ clearly linked to higher Chl-a in December 2019 (Supp. Figures S10, S11). Consequently



618 the region was a small CO₂ source of +0.07 (± 0.53) mmol.m⁻².d⁻¹ in December 2018 but a CO₂ sink in
619 December 2019 of -3.1 (± 1.0) mmol.m⁻².d⁻¹. Integrated over the region 25-30°S/50-60°E the carbon uptake
620 changed from a small CO₂ source in December 2018 of +0.019 TgC.month⁻¹ to a CO₂ sink in December 2019 of
621 -0.8 TgC.month⁻¹ (Supp Mat Figure S12) close to the estimate derived from observations in January 2020 (-1.0
622 TgC.month⁻¹). Over the period 1996-2018, the model evaluates each year a CO₂ source in December averaging
623 +0.12 (± 0.10) TgC.month⁻¹. This suggests that in late 2019 the CMEMS-LSCE-FFNN model did capture the
624 effect of the SEMB on pCO₂ and CO₂ fluxes, leading to a stronger regional CO₂ annual sink in 2019 (-8.8
625 TgC.yr⁻¹) compared to previous years (Figure 11).

626

627

628

629

630

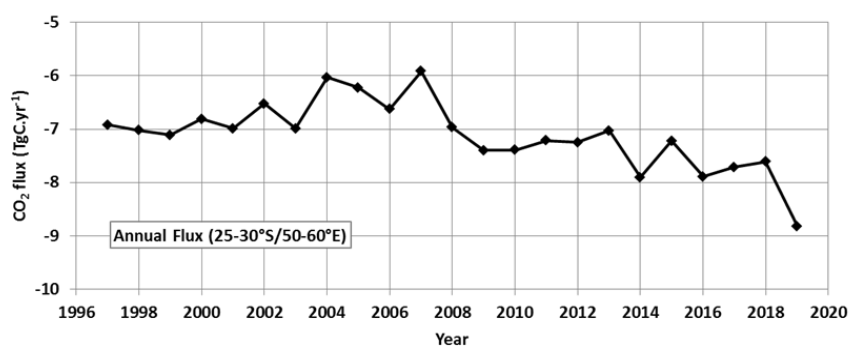
631

632

633

634

635



636 Figure 11: Annual air-sea CO₂ flux (TgC.yr⁻¹) in the South-Western Indian Ocean (region 25-30°S/50-60°E) for the period
637 1996-2019 from the CMEMS-LSCE-FFNN model. The carbon uptake progressively increased after 2007 with a maximum
638 CO₂ sink estimated in 2019 when the SEMB was particularly strong.

639

640 6. Conclusions

641

642 The new observations in the South-Western Indian Ocean presented here showed that the fCO₂ and C_T
643 concentrations in January 2020 were very low and far from normal conditions since 1991. This is explained by
644 the strong SEMB event that started in November 2019 in this region and was well developed in December 2019
645 and January 2020. Thanks to the continuous ocean color satellite data since 1997, the time-series of Chl-a in this
646 region showed that the bloom was particularly strong in austral summer 2019/2020. We suspect that prior to
647 1997, the SEMB has been less intense as suggested by *in-situ* fCO₂ data in 1991-1994 (Figure 2). We estimated
648 that the SEMB led to a regional carbon uptake of between -1.7 and -2.7 TgC.month⁻¹ in January 2020. The
649 variation of the regional ocean CO₂ sink due to the SEMB developed in late 2019 was also quantified with the
650 CMEMS-LSCE-FFNN model. Model results indicate a large anomaly in December 2019 that led to an annual
651 sink of -8.8 TgC.yr⁻¹, i.e. about 1 TgC.yr⁻¹ larger than previous years. The strong bloom in austral summer 2020
652 represents an interesting benchmark case to test models for a better understanding of the origin of the SEMB and
653 its impact on the regional ocean CO₂ sink. Future studies should target sensitivity analysis with complex
654 biogeochemical models including the CO₂ system, at different spatial resolution for the dynamics, and with (or
655 without) N₂ fixers (e.g. Monteiro et al 2010; Landolfi et al 2015; Paulsen et al 2017). This plankton functional
656 type is not yet included to models dedicated to this region (Srokosz et al 2015, Dilmahamod et al 2020). The new
657 fCO₂, C_T, A_T and N₂ fixation rate observations presented here along with historical data (e.g. SOCAT, Bakker et
658 al 2016, 2021, Figure 2) could serve as a validation to compare periods with or without bloom. In the future, if
659 the SEMB as observed in 2020 is more frequent or becomes a regular situation and if organic matter is exported



660 below the surface mixed layer, this could represent a negative feedback to the ocean carbon cycle, i.e. the ocean
661 sink would be enhanced. As already noted by several authors (e.g. Dilmahamod et al 2019) dedicated studies in
662 this region, including the sampling of plankton, nutrients (e. g. iron), but also the determination of rates (e.g. N₂-
663 fixation) etc... would be relevant to understand the processes controlling the SEMB and to evaluate its impact on
664 the biological carbon pump.
665

666 **Data availability**

667 Data used in this study are available in SOCAT (www.socat.info) for fCO₂ surface data, in GLODAP
668 (www.glodap.info) for water-column data, at NCEI/OCADS ([www.ncei.noaa.gov/access/ocean-carbon-data-
669 system/oceans/VOS_Program/OISO.html](http://www.ncei.noaa.gov/access/ocean-carbon-data-system/oceans/VOS_Program/OISO.html)) for A_T-C_T surface data, at Jas-ADCP
670 (<http://uhslc.soest.hawaii.edu/sadcp>) for ADCP data. The CMEMS-LSCE-FFNN model data are available at
671 E.U. Copernicus Marine Service Information (<https://resources.marine.copernicus.eu/products>).
672

673 **Authors contributions**

674 CLM and NM are co-Is of the ongoing OISO project. fCO₂, A_T and C_T data for OISO-30 were measured by
675 CLM, CL and CM and qualified by CLM and NM. Nutrients data for OISO-30 were measured and qualified by
676 CL. N₂-fix data for OISO-30 were measured and qualified by CR. CLM, NM, and JF qualified fCO₂, A_T and C_T
677 data for previous OISO cruises. MG and TTTC developed the CMEMS-LSCE-FFNN model and provided the
678 model results. NM started the analysis, wrote the draft of the manuscript and prepared the figures with
679 contributions from all authors.
680

681 **Competing interest**

682 The authors declare that they have no conflict of interest.
683

684 **Acknowledgments**

685 The OISO program was supported by the French institutes INSU (Institut National des Sciences de l'Univers)
686 and IPEV (Institut Polaire Paul-Emile Victor), OSU Ecce-Terra (at Sorbonne Université), and the French
687 program SOERE/Great-Gases. We thank the French oceanographic fleet ("Flotte océanographique française")
688 for financial and logistic support to the OISO program and the OISO-30 oceanographic campaign
689 (<https://doi.org/10.17600/18000679>). We thank the captains and crew of *R.R.V. Marion Dufresne* and the staff at
690 IFREMER, GENAVIR and IPEV. N₂ fixation analysis was also supported by the French Research Program
691 LEFE (Les Enveloppes Fluides et l'Environnement) through ITALIANO project and we thank Magloire
692 Mandeng-Yogo and Fethiye Cetin for the measurements performed at the ALYSES plate-form (OSU Ecce-
693 Terra). The development of the neural network model benefited from funding by the French INSU-GMMC
694 project "PPR-Green-Grog (grant no 5-DS-PPR-GGREGO), the EU H2020 project AtlantOS (grant no 633211),
695 as well as through the Copernicus Marine Environment Monitoring Service (project 83-CMEMS-TAC-MOB).
696 The Surface Ocean CO₂ Atlas (SOCAT, www.socat.info) is an international effort, endorsed by the International
697 Ocean Carbon Coordination Project (IOCCP), the Surface Ocean Lower Atmosphere Study (SOLAS) and the
698 Integrated Marine Biogeochemistry and Ecosystem Research program (IMBER), to deliver a uniformly quality-
699 controlled surface ocean CO₂ database.
700



701 **References**

702

703 Aminot, A. and R. K erouel: Dosage automatique des nutriments dans les eaux marines. M ethodes en flux
704 continu. Ed Ifremer-Quae, 188 p., ISBN-13 978-2-7592-0023-8, 2007

705

706 Bakker, D. C. E., Pfeil, B., Landa, C. S., Metzl, N., O'Brien, K. M., Olsen, A., Smith, K., Cosca, C., Harasawa,
707 S., Jones, S. D., Nakaoka, S.-I., Nojiri, Y., Schuster, U., Steinhoff, T., Sweeney, C., Takahashi, T., Tilbrook, B.,
708 Wada, C., Wanninkhof, R., Alin, S. R., Balestrini, C. F., Barbero, L., Bates, N. R., Bianchi, A. A., Bonou, F.,
709 Boutin, J., Bozec, Y., Burger, E. F., Cai, W.-J., Castle, R. D., Chen, L., Chierici, M., Currie, K., Evans, W.,
710 Featherstone, C., Feely, R. A., Fransson, A., Goyet, C., Greenwood, N., Gregor, L., Hankin, S., Hardman-
711 Mountford, N. J., Harlay, J., Hauck, J., Hoppema, M., Humphreys, M. P., Hunt, C. W., Huss, B., Ib anhez, J. S.
712 P., Johannessen, T., Keeling, R., Kitidis, V., K ortzinger, A., Kozyr, A., Krasakopoulou, E., Kuwata, A.,
713 Landsch tzer, P., Lauvset, S. K., Lef evre, N., Lo Monaco, C., Manke, A., Mathis, J. T., Merlivat, L., Millero, F.
714 J., Monteiro, P. M. S., Munro, D. R., Murata, A., Newberger, T., Omar, A. M., Ono, T., Paterson, K., Pearce, D.,
715 Pierrot, D., Robbins, L. L., Saito, S., Salisbury, J., Schlitzer, R., Schneider, B., Schweitzer, R., Sieger, R.,
716 Skjelvan, I., Sullivan, K. F., Sutherland, S. C., Sutton, A. J., Tadokoro, K., Telszewski, M., Tuma, M., Van
717 Heuven, S. M. A. C., Vandemark, D., Ward, B., Watson, A. J., and Xu, S.: A multi-decade record of high-
718 quality fCO₂ data in version 3 of the Surface Ocean CO₂ Atlas (SOCAT), Earth Syst. Sci. Data, 8, 383-413,
719 doi:10.5194/essd-8-383-2016, 2016.

720

721 Bakker, D. C. E. et al. Surface Ocean CO₂ Atlas Database Version 2021 (SOCATv2021) (NCEI Accession
722 0210711). NOAA National Centers for Environmental Information. Dataset. <https://doi.org/10.25921/4xkx-ss49>.
723 2021. Last Access 15/6/2021.

724

725 Bates, N. R., A. C. Pequignat, and C. L. Sabine: Ocean carbon cycling in the Indian Ocean: 1. Spatiotemporal
726 variability of inorganic carbon and air-sea CO₂ gas exchange, Global Biogeochem. Cycles, 20, GB3020,
727 doi:10.1029/2005GB002491, 2006.

728

729 Broull on, D., P erez, F. F., Velo, A., Hoppema, M., Olsen, A., Takahashi, T., Key, R. M., Tanhua, T., Santana-
730 Casiano, J. M., and Kozyr, A.: A global monthly climatology of oceanic total dissolved inorganic carbon: a
731 neural network approach, Earth Syst. Sci. Data, 12, 1725-1743, <https://doi.org/10.5194/essd-12-1725-2020>,
732 2020.

733

734 Chau, T. T. T., Gehlen, M., and Chevallier, F.: A seamless ensemble-based reconstruction of surface ocean pCO₂
735 and air-sea CO₂ fluxes over the global coastal and open oceans, Biogeosciences Discuss. [preprint],
736 <https://doi.org/10.5194/bg-2021-207>, in review, 2021.

737

738 Copin-Mont egut, C.: A new formula for the effect of temperature on the partial pressure of CO₂ in seawater.
739 *Marine Chemistry*, 25, 29-37. [https://doi.org/10.1016/0304-4203\(88\)90012-6](https://doi.org/10.1016/0304-4203(88)90012-6), 1988.

740

741 Copin-Mont egut, C.: A new formula for the effect of temperature on the partial pressure of CO₂ in seawater.
742 Corrigendum. *Marine Chemistry*, 27, 143-144. [https://doi.org/10.1016/0304-4203\(89\)90034-0](https://doi.org/10.1016/0304-4203(89)90034-0), 1989.



- 743
- 744 Coverly, S. C., Aminot, A., and R. K erouel: Nutrients in Seawater Using Segmented Flow Analysis, In: Practical
745 Guidelines for the Analysis of Seawater, Edited by: Oliver Wurl, CRC Press,
746 <https://doi.org/10.1201/9781420073072>, 2009.
- 747
- 748 de Ruijter, W. P. M., H. M. van Aken, E. J. Beier et al.: Eddies and dipoles around South Madagascar:
749 Formation, pathways and large-scale impacts, *Deep Sea Res., Part I*, 51, 383–400,
750 <https://doi.org/10.1016/j.dsr.2003.10.011>, 2004.
- 751
- 752 Dickson, A. G.: Standard potential of the reaction: $\text{AgCl(s)} + \frac{1}{2}\text{H}_2\text{(g)} = \text{Ag(s)} + \text{HCl(aq)}$, and the standard
753 acidity constant of the ion HSO_4^- in synthetic sea water from 273.15 to 318.15 K. *J. Chem. Thermodyn.* **22**:
754 113–127. doi:10.1016/0021-9614(90)90074-Z, 1990.
- 755
- 756 Dilmahamad, A. F., Penven, P., Aguiar-Gonz alez, B., Reason, C. J. C., & Hermes, J. C.: A new
757 definition of the South-East Madagascar Bloom and analysis of its variability. *Journal of Geophysical*
758 *Research: Oceans*, *124*, 1717–1735. <https://doi.org/10.1029/2018JC014582>, 2019
- 759
- 760 Dilmahamad, A. F., Penven, P., Aguiar-Gonzalez, B., Reason, C. J. C., & Hermes, J. C.: A model
761 investigation of the influences of the South-East Madagascar current on the South-East Madagascar bloom.
762 *Journal of Geophysical Research: Oceans*, *125*, e2019JC015761. <https://doi.org/10.1029/2019JC015761>, 2020.
- 763
- 764 Edmond, J. M.: High precision determination of titration alkalinity and total carbon dioxide content of sea water
765 by potentiometric titration, *Deep-Sea Res.*, *17*, 737–750, [https://doi.org/10.1016/0011-7471\(70\)90038-0](https://doi.org/10.1016/0011-7471(70)90038-0), 1970.
- 766
- 767 Fay, A. R., Gregor, L., Landsch tzer, P., McKinley, G. A., Gruber, N., Gehlen, M., Iida, Y., Laruelle, G. G.,
768 R odenbeck, C., and Zeng, J.: Harmonization of global surface ocean pCO_2 mapped products and their flux
769 calculations; an improved estimate of the ocean carbon sink, *Earth Syst. Sci. Data Discuss.* [preprint],
770 <https://doi.org/10.5194/essd-2021-16>, in review, 2021.
- 771
- 772 GMAO, Global Modeling and Assimilation Office: MERRA-2 tavgM_2d_flux_Nx: 2d, Monthly mean, Time-
773 Averaged, Single-Level, Assimilation, Surface Flux Diagnostics V5.12.4, Greenbelt, MD, USA, Goddard Earth
774 Sciences Data and Information Services Center (GES DISC), Accessed: [19/4/2021], 10.5067/0JRLVL8YV2Y4,
775 2015.
- 776
- 777 Gregor, L. and Gruber, N.: OceanSODA-ETHZ: a global gridded data set of the surface ocean carbonate system
778 for seasonal to decadal studies of ocean acidification, *Earth Syst. Sci. Data*, *13*, 777–808,
779 <https://doi.org/10.5194/essd-13-777-2021>, 2021.
- 780
- 781 Gruber, N., D. Clement, B. R. Carter, R. A. Feely, S. van Heuven, M. Hoppema, M. Ishii, R. M. Key, A. Kozyr,
782 S. K. Lauvset, C. Lo Monaco, J. T. Mathis, A. Murata, A. Olsen, F. F. Perez, C. L. Sabine, T. Tanhua, and R.
783 Wanninkhof: The oceanic sink for anthropogenic CO_2 from 1994 to 2007, *Science* vol. 363 (issue 6432), pp.
784 1193–1199. DOI: 10.1126/science.aau5153, 2019a
- 785



- 786 Gruber, N., Clement, D., Carter, B. R., Feely, R. A., Heuven, S. van, Hoppema, M., Ishii, M., Key, R. M.,
787 Kozyr, A., Lauvset, S. K., Lo Monaco, C., Mathis, J. T., Murata, A., Olsen, A., Perez, F. F., Sabine, C. L.,
788 Tanhua, T. and Wanninkhof, R.: The oceanic sink for anthropogenic CO₂ from 1994 to 2007 - the data (NCEI
789 Accession 0186034). NOAA National Centers for Environmental Information. Dataset.
790 <https://doi.org/10.25921/wdn2-pt10>, 2019b [last acces 17/02/2020].
791
- 792 Hörstmann, C., Raes, E. J., Buttigieg, P. L., Lo Monaco, C., John, U., and Waite, A. M.: Hydrographic fronts
793 shape productivity, nitrogen fixation, and microbial community composition in the southern Indian Ocean and
794 the Southern Ocean, *Biogeosciences*, 18, 3733–3749, <https://doi.org/10.5194/bg-18-3733-2021>, 2021.
795
- 796 Huhn, F., A. von Kameke, V. Pérez-Muñuzuri, M. J. Olascoaga, and F. J. Beron-Vera: The impact of advective
797 transport by the South Indian Ocean countercurrent on the Madagascar bloom, *Geophys. Res. Lett.*, 39,
798 doi:10.1029/2012GL051246, 2012.
799
- 800 Keppler, L., Landschützer, P., Gruber, N., Lauvset, S. K., & Stemmler, I.: Seasonal carbon dynamics in the near-
801 global ocean. *Global Biogeochemical Cycles*, 34, e2020GB006571. doi:10.1029/2020GB006571, 2020.
802
- 803 Ko, Y. H., Lee, K., Takahashi, T., Karl, D. M., Kang, S.-H., & Lee, E.: Carbon-based estimate of nitrogen
804 fixation-derived net community production in N-depleted ocean gyres. *Global Biogeochemical Cycles*, 32.
805 Doi:10.1029/2017GB005634, 2018.
806
- 807 Landolfi, A., Koeve, W., Dietze, H., Kähler, P., & Oschlies, A.: A new perspective on environmental controls of
808 marine nitrogen fixation. *Geophysical Research Letters*, 42, 4482–4489. <https://doi.org/10.1002/2015GL063756>,
809 2015.
810
- 811 Landschützer P., N. Gruber, and D. Bakker: Decadal variations and trends of the global ocean carbon sink,
812 *Global Biogeochem. Cycles*, 30, doi:10.1002/2015GB005359, 2016.
813
- 814 Lauvset, S. K, R. M. Key, A. Olsen, S. van Heuven, A. Velo, X. Lin, C. Schirnick, A. Kozyr, T. Tanhua, M.
815 Hoppema, S. Jutterström, R. Steinfeldt, E. Jeansson, M. Ishii, F. F. Pérez, T. Suzuki & S. Watelet: A new global
816 interior ocean mapped climatology: the 1°x1° GLODAP version 2. *Earth Syst. Sci. Data*, 8, 325-340,
817 doi:10.5194/essd-8-325-2016, 2016.
818
- 819 Lauvset, S. K., Lange, N., Tanhua, T., Bittig, H. C., Olsen, A., Kozyr, A., Álvarez, M., Becker, S., Brown, P. J.,
820 Carter, B. R., Cotrim da Cunha, L., Feely, R. A., van Heuven, S., Hoppema, M., Ishii, M., Jeansson, E.,
821 Jutterström, S., Jones, S. D., Karlsen, M. K., Lo Monaco, C., Michaelis, P., Murata, A., Pérez, F. F., Pfeil, B.,
822 Schirnick, C., Steinfeldt, R., Suzuki, T., Tilbrook, B., Velo, A., Wanninkhof, R., Woosley, R. J., and Key, R. M.:
823 An updated version of the global interior ocean biogeochemical data product, GLODAPv2.2021, *Earth Syst. Sci.*
824 *Data Discuss.* [preprint], <https://doi.org/10.5194/essd-2021-234>, in review, 2021a.
825
- 826 Lauvset, Siv K.; Lange, Nico; Tanhua, Toste; Bittig, Henry C.; Olsen, Are; Kozyr, Alex; Álvarez, Marta;
827 Becker, Susan; Brown, Peter J.; Carter, Brendan R.; Cotrim da Cunha, Leticia; Feely, Richard A.; van Heuven,
828 Steven M. A. C.; Hoppema, Mario; Ishii, Masao; Jeansson, Emil; Jutterström, Sara; Jones, Steve D.; Karlsen,



- 829 Maren K.; Lo Monaco, Claire; Michaelis, Patrick; Murata, Akihiko; Pérez, Fiz F.; Pfeil, Benjamin; Schirnack,
830 Carsten; Steinfeldt, Reiner; Suzuki, Toru; Tilbrook, Bronte; Velo, Antón; Wanninkhof, Rik; Woosley, Ryan J.;
831 Key, Robert M.: Global Ocean Data Analysis Project version 2.2021 (GLODAPv2.2021) (NCEI Accession
832 0237935). [subset used GLODAPv2.2021_Indian_Ocean.cvs]. NOAA National Centers for Environmental
833 Information. Dataset. <https://doi.org/10.25921/ttgg-n825>, 2021b. Accessed 2/8/2021.
834
- 835 Lee, K., Wanninkhof, R., Feely, R. A., Millero, F. J., & Peng, T. H.: Global relationships of total inorganic
836 carbon with temperature and nitrate in surface seawater. *Global Biogeochemical Cycles*, 14(3), 979–994.
837 <https://doi.org/10.1029/1998GB001087>, 2000.
838
- 839 Lee, K., Karl, D. M., Wanninkhof, R., & Zhang, J. Z.: Global estimates of net carbon production in the nitrate-
840 depleted tropical and subtropical oceans. *Geophysical Research Letters*, 29(19), 1907.
841 <https://doi.org/10.1029/2001GL014198>, 2002.
842
- 843 Lee, K., Tong, L.T., Millero, F.J., Sabine, C.L., Dickson, A.G., Goyet, C., Park, G.H., Wanninkhof, R., Feely,
844 R.A., and Key, R.M.: Global relationships of total alkalinity with salinity and temperature in surface waters of
845 the world's oceans. *Geophys. Res. Lett.* 33, L19605. doi10.1029/2006GL027207, 2006.
846
- 847 Lévy, M., Shankar, D., André, J.M., Shenoi, S. S., Durand, F., & de Boyer Montegut, C.: Basin-wide seasonal
848 evolution of the Indian Ocean's phytoplankton blooms. *Journal of Geophysical Research*, 112, C12014.
849 <https://doi.org/10.1029/2007JC004090>, 2007.
850
- 851 Lewis E. and D. W. R. Wallace: Program developed for CO₂ system calculations. ORNL/CDIAC-105. Carbon
852 Dioxide Information Analysis Center, Oak Ridge National Laboratory, US. Dept. of Energy, Oak Ridge, TN,
853 1998.
854
- 855 Lo Monaco, C. and N. Metzl: Surface underway measurements of partial pressure of carbon dioxide (pCO₂),
856 salinity, temperature and other associated parameters during the R/V Marion Dufresne OISO-30 cruise
857 (EXPOCODE 35MV20200106) in Indian Ocean from 2020-01-06 to 2020-02-01 (NCEI Accession 0223954).
858 [indicate subset used]. NOAA National Centers for Environmental Information. Dataset.
859 <https://www.ncei.noaa.gov/archive/accession/0223954>, 2021. Accessed 15-01-2021.
860
- 861 Lo Monaco, C., Metzl, N., Fin, J., Mignon, C., Cuet, P., Douville, E., Gehlen, M., Trang Chau, T.T., and
862 Tribollet, A.: Distribution and long-term change of the sea surface carbonate system in the Mozambique Channel
863 (1963-2019), *Deep-Sea Research Part II*, <https://doi.org/10.1016/j.dsr2.2021.104936>, 2021.
864
- 865 Longhurst, A.: A major seasonal phytoplankton bloom in the Madagascar Basin. *Deep-Sea Research Part I: Oceanographic Research Papers*, 48(11), 2413–2422. [https://doi.org/10.1016/S0967-0637\(01\)00024-3](https://doi.org/10.1016/S0967-0637(01)00024-3), 2001.
866
867
- 868 Louanchi, F., N. Metzl, and A. Poisson : Modelling the monthly sea surface fCO₂ fields in the Indian Ocean.
869 *Marine Chemistry*, 55, 265-279. [https://doi.org/10.1016/S0304-4203\(96\)00066-7](https://doi.org/10.1016/S0304-4203(96)00066-7), 1996.
870



- 871 Lueker, T.J., Dickson, A.G., Keeling, C.D.: Ocean pCO₂ calculated from dissolved inorganic carbon,
872 alkalinity, and equations for K-1 and K-2: validation based on laboratory measurements of CO₂ in gas and
873 seawater at equilibrium. *Marine Chemistry* 70, 105-119. [https://doi.org/10.1016/S0304-4203\(00\)00022-0](https://doi.org/10.1016/S0304-4203(00)00022-0), 2000.
874
- 875 Lutjeharms, J.R.E.: Remote sensing corroboration of retroflection of the East Madagascar Current. *Deep Sea*
876 *Res.* 35, 2045–2050. [https://doi.org/10.1016/0198-0149\(88\)90124-0](https://doi.org/10.1016/0198-0149(88)90124-0), 1988.
877
- 878 Menezes, V. V., H. E. Phillips, A. Schiller, N. L. Bindoff, C. M. Domingues, and M. L. Vianna: South Indian
879 countercurrent and associated fronts, *J. Geophys. Res. Oceans*, 119, 6763–6791, doi:10.1002/2014JC010076,
880 2014.
881
- 882 Metzl, N., A. Poisson, F. Louanchi, C. Brunet, B. Schauer & B. Bres: Spatio-temporal distributions of air-sea
883 fluxes of CO₂ in the Indian and Antarctic oceans, *Tellus B: Chemical and Physical Meteorology*, 47:1-2, 56-69,
884 doi:10.3402/tellusb.v47i1-2.16006, 1995.
885
- 886 Metzl, N., F. Louanchi, and A. Poisson: Seasonal and interannual variations of sea surface carbon dioxide in the
887 subtropical indian ocean. *Marine Chemistry*, 60, 131-146. [https://doi.org/10.1016/S0304-4203\(98\)00083-8](https://doi.org/10.1016/S0304-4203(98)00083-8),
888 1998.
889
- 890 Metzl, N., C. Brunet, A. Jabaud-Jan, A. Poisson and B. Schauer: Summer and winter air-sea CO₂ fluxes in the
891 Southern Ocean *Deep Sea Res I*, 53, 1548-1563, doi:10.1016/j.dsr.2006.07.006, 2006.
892
- 893 Metzl, N.: Decadal increase of oceanic carbon dioxide in the Southern Indian Ocean surface waters (1991-2007).
894 *Deep Sea Research Part II: Topical Studies in Oceanography*, 56, 8–10, 607-619.
895 <https://doi.org/10.1016/j.dsr2.2008.12.007>, 2009.
896
- 897 Millero, F. J., Lee, K. and Roche, M.: Distribution of alkalinity in the surface waters of the major oceans. *Mar.*
898 *Chem.* 60, 111–130. [https://doi.org/10.1016/S0304-4203\(97\)00084-4](https://doi.org/10.1016/S0304-4203(97)00084-4), 1998.
899
- 900 Monteiro, F. M., M. J. Follows, and S. Dutkiewicz: Distribution of diverse nitrogen fixers in the global ocean,
901 *Global Biogeochem. Cycles*, 24, GB3017, doi:10.1029/2009GB003731, 2010.
902
- 903 Montoya, J. P., Voss, M., Kahler, P., and Capone, D. G.: A simple, high-precision, high-sensitivity tracer assay
904 for N₂ fixation, *Appl. Environ. Microb.*, 62, 986–993, <https://doi.org/10.1128/aem.62.3.986-993.1996>, 1996
905
- 906 Murata, A., Kumamoto, Y., Sasaki, K., Watanabe, S., & Fukasawa, M.: Decadal increases in anthropogenic CO₂
907 along 20°S in the South Indian Ocean. *Journal of Geophysical Research*, 115, C12055.
908 <https://doi.org/10.1029/2010JC006250>, 2010.
909
- 910 Orr, J. C., J.-M. Epitalon, A. G. Dickson and J.-P. Gattuso: Routine uncertainty propagation for the marine
911 carbon dioxide system, *Marine Chemistry*, Vol. 207, 84-107, doi:10.1016/j.marchem.2018.10.006, 2018.
912



- 913 Palastanga, V., P. J. van Leeuwen, M. W. Schouten, and W. P. M. de Ruijter: Flow structure and variability in
914 the subtropical Indian Ocean: Instability of the South Indian Ocean Countercurrent, *J. Geophys. Res.*, 112,
915 C01001, doi:10.1029/2005JC003395, 2007.
- 916
- 917 Paulsen, H., Ilyina, T., Six, K. D., & Stemmler, I.: Incorporating a prognostic representation of marine nitrogen
918 fixers into the global ocean biogeochemical model HAMOCC. *Journal of Advances in Modeling Earth Systems*,
919 9, 438–464. <https://doi.org/10.1002/2016MS000737>, 2017.
- 920
- 921 Peng, T H., Wanninkhof, R., Bullister, J. *et al.*: Quantification of decadal anthropogenic CO₂ uptake in the ocean
922 based on dissolved inorganic carbon measurements. *Nature*, 396, 560–563. doi:10.1038/25103, 1998.
- 923
- 924 Pfeil, B., Olsen, A., Bakker, D. C. E., Hankin, S., Koyuk, H., Kozyr, A., Malczyk, J., Manke, A., Metzl, N.,
925 Sabine, C. L., Akl, J., Alin, S. R., Bates, N., Bellerby, R. G. J., Borges, A., Boutin, J., Brown, P. J., Cai, W.-J.,
926 Chavez, F. P., Chen, A., Cosca, C., Fassbender, A. J., Feely, R. A., González-Dávila, M., Goyet, C., Hales,
927 B., Hardman-Mountford, N., Heinze, C., Hood, M., Hoppema, M., Hunt, C. W., Hydes, D., Ishii, M.,
928 Johannessen, T., Jones, S. D., Key, R. M., Körtzinger, A., Landschützer, P., Lauvset, S. K., Lefèvre, N.,
929 Lenton, A., Lourantou, A., Merlivat, L., Midorikawa, T., Mintrop, L., Miyazaki, C., Murata, A., Nakadate, A.,
930 Nakano, Y., Nakaoka, S., Nojiri, Y., Omar, A. M., Padin, X. A., Park, G.-H., Paterson, K., Perez, F. F., Pierrot,
931 D., Poisson, A., Ríos, A. F., Santana-Casiano, J. M., Salisbury, J., Sarma, V. V. S. S., Schlitzer, R.,
932 Schneider, B., Schuster, U., Sieger, R., Skjelvan, I., Steinhoff, T., Suzuki, T., Takahashi, T., Tedesco, K.,
933 Telszewski, M., Thomas, H., Tilbrook, B., Tjiputra, J., Vandemark, D., Veness, T., Wanninkhof, R., Watson,
934 A. J., Weiss, R., Wong, C. S., and Yoshikawa-Inoue, H.: A uniform, quality controlled Surface Ocean CO₂ Atlas
935 (SOCAT), *Earth Syst. Sci. Data*, 5, 125–143, doi:10.5194/essd-5-125-2013, 2013.
- 936
- 937 Pierella Karlusich, J.J., Pelletier, E., Lombard, F. *et al.*: Global distribution patterns of marine nitrogen-fixers by
938 imaging and molecular methods. *Nat. Commun.*, 12, 4160. doi:10.1038/s41467-021-24299-y, 2021.
- 939
- 940 Pierrot, D., E. Lewis, and D. W. R. Wallace: MS Excel Program Developed for CO₂ System Calculations
941 ORNL/CDIAC-105, Carbon Dioxide Inf. Anal. Cent., Oak Ridge Natl. Lab., U. S. Dept. of Energy, Oak Ridge,
942 Tenn., 2006.
- 943
- 944 Poisson, A., Metzl, N., Brunet, C., Schauer, B., Bres, B., Ruiz-Pino, D., and Louanchi, F.: Variability of sources
945 and sinks of CO₂ in the western Indian and southern oceans during the year 1991, *J. Geophys. Res.*, 98(C12),
946 22759– 22778, doi:10.1029/93JC02501, 1993.
- 947
- 948 Poulton, A. J., M. C. Stinchcombe, and G. D. Quartly: High numbers of Trichodesmium and diazotrophic
949 diatoms in the southwest Indian Ocean, *Geophys. Res. Lett.*, 36, L15610, doi:10.1029/2009GL0397179, 2009.
- 950
- 951 Qi, L., C. Hu, K. Mikelsons, M. Wang, V. Lance, S. Sun, B. B. Barnes, J. Zhao, and D. Van der Zande: In search
952 of floating algae and other organisms in global oceans and lakes. *Remote Sensing of Environment*, 239, 111659,
953 <https://doi.org/10.1016/j.rse.2020.111659>, 2020.
- 954



- 955 Raj, R. P., Peter, B. N., & Pushpadas, D.: Oceanic and atmospheric influences on the variability of
956 phytoplankton bloom in the Southwestern Indian Ocean. *Journal of Marine Systems*, 82(4), 217–229.
957 <https://doi.org/10.1016/j.jmarsys.2010.05.009>, 2010.
958
- 959 Sabine, C. L., R. Wanninkhof, R. M. Key, C. Goyet, and F. J. Millero: Seasonal CO₂ fluxes in the tropical and
960 subtropical Indian Ocean, *Mar. Chem.*, 72, 33–53. [https://doi.org/10.1016/S0304-4203\(00\)00064-5](https://doi.org/10.1016/S0304-4203(00)00064-5), 2000.
961
- 962 Schlitzer, R., 2013. Ocean Data View, <http://odv.awi.de>.
963
- 964 Siedler, G., M. Rouault, and J. R. E. Lutjeharms: Structure and origin of the subtropical South Indian Ocean
965 Countercurrent, *Geophys. Res. Lett.*, 33, L24609, doi:10.1029/2006GL027399, 2006.
966
- 967 Srokosz, M. A., Quartly, G. D., & Buck, J. J. H.: A possible plankton wave in the Indian Ocean. *Geophysical*
968 *Research Letters*, 31, L13301. <https://doi.org/10.1029/2004GL019738>, 2004.
969
- 970 Srokosz, M. A., & Quartly, G. D.: The Madagascar Bloom: A serendipitous study. *Journal of Geophysical*
971 *Research: Oceans*, 118, 14–25. <https://doi.org/10.1029/2012JC008339>, 2013.
972
- 973 Srokosz, M. A., Robinson, J., McGrain, H., Popova, E. E., & Yool, A.: Could the Madagascar bloom be fertilized
974 by Madagascan iron? *Journal of Geophysical Research: Oceans*, 120, 5790–5803.
975 <https://doi.org/10.1002/2015JC011075>, 2015.
976
- 977 Takahashi, T., Olafsson, J., Goddard, J. G., Chipman, D. W., and Sutherland, S. C.: Seasonal variation of CO₂
978 and nutrients in the high-latitude surface oceans: A comparative study, *Global Biogeochem. Cycles*, 7(4), 843–
979 878, doi:10.1029/93GB02263, 1993.
980
- 981 Takahashi, T., Sutherland, S. C., Sweeney, C., Poisson, A., Metzl, N., Tilbrook, B., Bates, N., Wanninkhof, R.,
982 Feely, R. A., Sabine, C., Olafsson, J., and Nojiri, Y.: Global Sea-Air CO₂ Flux Based on Climatological Surface
983 Ocean pCO₂, and Seasonal Biological and Temperature Effect. *Deep-Sea Res. II*, 49, 9-10, 1601-1622,
984 [https://doi.org/10.1016/S0967-0645\(02\)00003-6](https://doi.org/10.1016/S0967-0645(02)00003-6), 2002.
985
- 986 Takahashi, T., Sutherland, S. C., Wanninkhof, R., Sweeney, C., Feely, R. A., Chipman, D. W., Hales, B.,
987 Friederich, G., Chavez, F., Sabine, C., Watson, A. J., Bakker, D. C., Schuster, U., Metzl, N., Yoshikawa-Inoue,
988 H., Ishii, M., Midorikawa, T., Nojiri, Y., Körtzinger, A., Steinhoff, T., Hoppema, M., Olafsson, J., Arnarson, T.
989 S., Tilbrook, B., Johannessen, T., Olsen, A., Bellerby, R., Wong, C., Delille, B., Bates, N., and de Baar, H. J.:
990 Climatological mean and decadal change in surface ocean pCO₂, and net sea air CO₂ flux over the global
991 oceans. *Deep-Sea Res. II*, 56(8-10), 554–577, <http://dx.doi.org/10.1016/j.dsr2.2008.12.009>, 2009.
992
- 993 Takahashi, T., Sutherland, S. C., Chipman, D. W., Goddard, J. G., Ho, C., Newberger, T., Sweeney, C. and
994 Munro, D. R.: Climatological distributions of pH, pCO₂, total CO₂, alkalinity, and CaCO₃ saturation in the
995 global surface ocean, and temporal changes at selected locations. *Marine Chemistry*, 164, 95–125,
996 doi:10.1016/j.marchem.2014.06.004, 2014.
997



- 998 Tang, W., & Cassar, N.: Data-driven modeling of the distribution of diazotrophs in the global
999 ocean. *Geophysical Research Letters*, 46, 12,258–12,269. <https://doi.org/10.1029/2019GL084376>, 2019.
1000
- 1001 Tang, W., Li, Z., & Cassar, N.: Machine learning estimates of global marine nitrogen fixation. *Journal of*
1002 *Geophysical Research: Biogeosciences*, 124, 717–730. <https://doi.org/10.1029/2018JG004828>. 2019.
1003
- 1004 Touratier, F., Azouzi, L. and Goyet, C.: CFC-11, $\Delta 14C$ and 3H tracers as a means to assess anthropogenic CO₂
1005 concentrations in the ocean. *Tellus B*, 59(2), 318–325, doi:10.1111/j.1600-0889.2006.00247.x, 2007.
1006
- 1007 Uppström, L. R.: The boron/chlorinity ratio of deep-sea water from the Pacific Ocean, *Deep Sea Research and*
1008 *Oceanographic Abstracts*, 21, 161–162, [https://doi.org/10.1016/0011-7471\(74\)90074-6](https://doi.org/10.1016/0011-7471(74)90074-6), 1974.
1009
- 1010 Uz, B. M.: What causes the sporadic phytoplankton bloom southeast of Madagascar? *Journal of Geophysical*
1011 *Research*, 112, C09010. <https://doi.org/10.1029/2006JC003685>, 2007
1012
- 1013 Wanninkhof, R.: Relationship between wind speed and gas exchange over the ocean, *J. Geophys. Res.*, 97(C5),
1014 7373–7382, doi:10.1029/92JC00188, 1992.
1015
- 1016 Wanninkhof, R.: Relationship between wind speed and gas exchange over the ocean revisited, *Limnol.*
1017 *Oceanogr. Methods*, 12, 351–362, doi:10.4319/lom.2014.12.351, 2014.
1018
- 1019 Weiss, R. F.: Carbon dioxide in water and seawater: The solubility of a non-ideal gas, *Mar. Chem.*, 2, 203–215,
1020 doi:10.1016/0304-4203(74)90015-2, 1974.
1021
- 1022 Weiss, R. F. and Price, B. A.: Nitrous oxide solubility in water and seawater. *Marine Chemistry*, 8(4), 347–359,
1023 doi:10.1016/0304-4203(80)90024-9, 1980.
1024
- 1025 Westberry, T. K., and D. A. Siegel: Spatial and temporal distribution of *Trichodesmium* blooms in the world's
1026 oceans, *Global Biogeochem. Cycles*, 20, GB4016, doi:10.1029/2005GB002673, 2006.
1027
- 1028 Wilson, C., and X. Qiu: Global distribution of summer chlorophyll blooms in the oligotrophic gyres, *Prog.*
1029 *Oceanogr.*, 78, 107–134. <https://doi.org/10.1016/j.pocean.2008.05.002>, 2008
1030
- 1031 Zeng, J., Matsunaga, T., Saigusa, N., Shirai, T., Nakaoka, S.-I., and Tan, Z.-H.: Technical note: Evaluation of
1032 three machine learning models for surface ocean CO₂ mapping, *Ocean Sci.*, 13, 303–313, doi:10.5194/os-13-303-
1033 2017, 2017.